Engineering Applications of Artificial Intelligence 160 (2025) 111753

Contents lists available at ScienceDirect

Engineering Applications of Artificial Intelligence

journal homepage: www.elsevier.com/locate/engappai

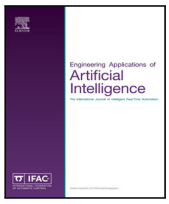

Research paper

Computationally efficient multi-objective optimization of an interior permanent magnet synchronous machine using neural networks

Mitja Garmut [a,*], Simon Steentjes [b], Martin Petrun [a]

[a] Institute of Electrical Power Engineering, FERI, University of Maribor, Koroška cesta 46, Maribor, 2000, Slovenia
[b] Institute of Electrical Machines, RWTH Aachen University, Schinkelstraße 4, Aachen, 52062, Germany

ARTICLE INFO

Keywords:
Interior permanent magnet synchronous machine
Artificial neural network
Meta-model
Multi-objective optimization
Finite element method

ABSTRACT

Improving the power density of an interior permanent magnet synchronous machine requires a complex and comprehensive approach that includes electromagnetic and thermal aspects. To achieve that, a multi-objective optimization of the machine's geometry was performed according to selected key performance indicators by using numerical and analytical models. The primary objective of this research was to create a computationally efficient and accurate alternative to a direct finite element method-based optimization. By integrating artificial neural networks as meta-models, we aimed to demonstrate their performance in comparison to existing State-of-the-Art approaches. The artificial neural network approach achieved a nearly 20-fold reduction compared with the finite element method-based approach in computation time while maintaining accuracy, demonstrating its effectiveness as a computationally efficient alternative. The obtained artificial neural network can also be reused for different optimization scenarios and for iterative fine-tuning, further reducing the computation time. To highlight the advantages and limitations of the proposed approach, a multi-objective optimization scenario was performed, which increased the power-to-mass ratio by 16.5%.

1. Introduction

Electrical machines are one of the cornerstones of our modern society, generating electrical energy and powering home appliances, power tools, electric vehicles, and industry equipment. In electric vehicles and power tools, the Interior Permanent Magnet Synchronous Machine (IPMSM) is preferred for its superior power density and efficiency (Husain et al., 2021; Zheng et al., 2022). The performance of an IPMSM is measured through machine Key Performance Indicators (KPIs), such as power, efficiency, cost, mass,... (Parekh et al., 2021). The KPIs provide a comprehensive overview of the machine's performance. The most efficient method for numerically computing KPIs is through the use of State-of-the-Art Finite Element Method (FEM) simulations, complemented by various post-processing evaluations (Bilgin et al., 2019; Sizov et al., 2012). This allows for accurate multiphysics performance evaluations, including the machine's nonlinear behavior. To achieve the best possible design based on selected KPIs, it is essential to perform a detailed Multi-Objective Optimization (MOO), as shown, e.g., in Parekh et al. (2022), Lucchini et al. (2022), Sun et al. (2021), Parekh et al. (2023a) and Vuković et al. (2024). This process should address multiple objectives, incorporate various constraints, and involve a carefully chosen set of parameters, to cover the entire search space comprehensively.

Given the intensive computational demands and the time-consuming nature of FEM-based numerical evaluations, direct optimization is impractical on standard computers. Computation and time efficiency are critical factors in the MOO process. If not approached adequately, optimization tasks can extend for weeks or even longer. Different approaches can be undertaken to overcome this problem. Meta-models are often employed to address this problem by limiting the number of FEM evaluations and training the models to predict the whole search space. Meta-models can be built by using the Kriging model (Sun et al., 2021; Zhao et al., 2018), response surface methods (Brown and Lorenz, 2007), and others (Pech et al., 2019). In recent years, the development of meta-models has increasingly incorporated machine-learning techniques as showcased in Sasaki and Igarashi (2019), Parekh et al. (2023b), Li et al. (2021), Parekh et al. (2023a), Brescia et al. (2021), Khan et al. (2020a), Sasaki et al. (2022), Lei et al. (2017) and Shimizu (2024). Meta-models can be employed to predict the KPIs directly (Parekh et al., 2023a) or only parts of it (Parekh et al., 2023b). In the presented research, Artificial Neural Networks (ANNs) were chosen as meta-models because they effectively capture nonlinear effects like saturation and cross-coupling in electric machine design (Li et al., 2021).

* Corresponding author.
E-mail address: mitja.garmut@um.si (M. Garmut).

https://doi.org/10.1016/j.engappai.2025.111753
Received 6 November 2024; Received in revised form 15 May 2025; Accepted 8 July 2025
Available online 25 July 2025

The primary objective of this study was to develop a computationally efficient MOO to optimize already high-performing IPMSMs. Consequently, the study focused on the following key goals:

1. To improve the MOO process in terms of computational complexity, i.e., to allow the discussed MOO on standard computers by incorporating ANN-based meta-models of the machine, which are trained on a reasonable volume of training data.
2. To evaluate the proposed ANN-based meta-model against State-of-the-Art approaches, including direct MOO with an integrated FEM model and the Kriging meta-model.
3. To apply the developed computationally efficient MOO to enhance the power-to-cost ratio of an already high-performing IPMSM within a complex mechatronic system and to identify the most suitable machine design from a set of optimal solutions.
4. To incorporate both electromagnetic and thermal aspects into the machine design evaluation to achieve an optimal design that balances both physical domains.

A novel approach consisting of ANN-based meta-models combined with analytical models of the IPMSM to predict specific KPIs was developed. The trained ANNs predicted the nonlinear characteristics of the IPMSM (i.e., flux linkages and torque) in selected Operating Points (OPs) with respect to the change of the geometry of the iron core's cross-section. Alternatively, Parekh et al. (2023b) employed a single deep neural network to predict numerical values of FEM solutions for KPI evaluation. In contrast, the approach presented in this study requires significantly less training data for the meta-models used in MOO, which can be generated on standard computers.

Direct FEM-based optimization is computationally expensive. By integrating trained ANNs into the optimization process, computational costs are significantly reduced while maintaining accuracy. This approach also allows for the reuse of trained ANNs in similar optimization problems or for iterative fine-tuning of optimization scenarios, enhancing versatility. The ANN-based approach was also compared to the widely used Kriging meta-model, a State-of-the-Art method for predicting electric machine performance.

In the MOO, we also considered thermal aspects of the IPMSM design to guarantee that the optimized design respected the prescribed thermal limits. This design aspect is oftentimes overlooked within optimizations. A two-objective optimization scenario was performed to showcase the effectiveness of the presented ANN-based meta-model MOO approach, where the KPIs power and mass were optimized.

This paper is organized as follows. Section 2 presents the theoretical background where the MOO setup is presented. In Section 3, the generation of FEM numerical data is presented. The implementation of ANN-based meta-models and the implementation of the MOO are presented in Sections 4 and 5, respectively. In Section 6, the results are presented. Section 7 highlights the conclusions.

2. Theoretical background

2.1. Problem statement

Enhancing high-performing and efficient IPMSMs poses a challenge, as modifications in one aspect often lead to compromises in another (Bramerdorfer et al., 2018). To overcome this problem, simultaneous optimization of different aspects of the IPMSM must be employed. This approach is known as MOO, resulting in a set of optimal solutions, i.e., the Pareto front (Li et al., 2023). The MOO is generally defined by (1),

$$\begin{aligned} \min_{\boldsymbol{x}} \quad & \mathcal{F}_i(\boldsymbol{x}),\ i = 1, \dots, N_{\mathcal{F}} \\ \text{subject to} \quad & \mathcal{G}_j(\boldsymbol{x}) \leq 0,\ j = 1, \dots, N_{\mathcal{G}} \\ & \mathcal{H}_k(\boldsymbol{x}) = 0,\ k = 1, \dots, N_{\mathcal{H}} \\ & \boldsymbol{x}_{\mathrm{L}} \leq \boldsymbol{x} \leq \boldsymbol{x}_{\mathrm{U}} \end{aligned} \tag{1}$$

where $\mathcal{F}_i(\boldsymbol{x})$ is the i-th objective (also called cost) function, $\mathcal{G}_j(\boldsymbol{x})$ is the j-th inequality constraint function, $\mathcal{H}_k(\boldsymbol{x})$ is the k-th equality constraint function, and the design search space is defined by a vector of optimization design variables $\boldsymbol{x}$ and their lower and upper limits, i.e., $\boldsymbol{x}_{\mathrm{L}}$ and $\boldsymbol{x}_{\mathrm{U}}$, respectively. It is important to note that feasible IPMSM designs are entirely characterized by a vector of design variables $\boldsymbol{x}$ (constrained within appropriate limits $\boldsymbol{x}_{\mathrm{L}}$ and $\boldsymbol{x}_{\mathrm{U}}$) and with fixed design parameters, which remain constant throughout the optimization process.

The main object to be optimized was an IPMSM that operates within a complex mechatronic system, i.e., a high-performance handheld power tool. The observed system consists of several subsystems that include energy storage, power electronics, the electric machine (i.e., the discussed IPMSM), a control subsystem, a gearbox, a housing, and a shared cooling system (Mohanraj et al., 2022; Garmut et al., 2024b). The initial system is thermally well balanced, i.e., the cooling system is adequately designed to handle the produced heat of all components under allowable (i.e., normal) operating conditions. The initial system is further well-defined mechanically and electrically, i.e., the speed range of the tool and the voltage level of the battery system are prescribed. Lastly, it is important to note that in an industrial environment the production processes and the connected costs introduce several rigid limitations for the technical improvement of products, where, e.g., a small change in the design of a component is not feasible commercially because it would require, e.g., a different production process or a new production tool. Consequently, a strict limitation was imposed in this research: all other components of the mechatronic system remain unchanged, with only the design of the IPMSM allowed to vary within specified constraints.

2.2. Parametrization of IPMSM designs

The discussed reference electrical machine is an IPMSM with 3-phase, 6-slot, 4-pole, Δ-connected fractional slot non-overlapping winding, and tangential oriented interior magnets. The presented machine utilizes high-temperature-resistant Nd-Fe-B magnets, ensuring stable performance under elevated temperature. The stator and rotor iron cores are made of non-oriented electrical steel with a thickness of 0.35 mm, a standard choice in high-performance electric machines. The design of the IPMSM typically allows for a 2D description of the electromagnetic problem (Pechlivanidou et al., 2019). To effectively implement the electromagnetic problem within an optimization procedure, the cross-section of the machine was parametrized. The parametrized geometry is presented in Fig. 1, where due to the circular symmetry only a part (i.e., $\frac{1}{12}$ of the stator and $\frac{1}{8}$ of the rotor) of the cross-section is shown.

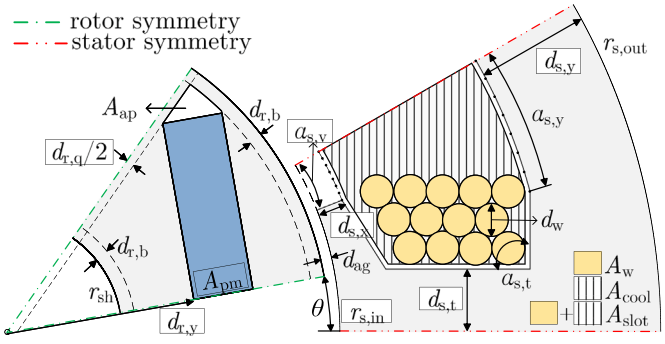

Fig. 1. Parametrized geometry of the analyzed IPMSM.

The design of the stator's iron core cross-section was defined by the following geometric parameters: outer radius $r_{\mathrm{s,out}}$, inner radius $r_{\mathrm{s,in}}$, yoke width $d_{\mathrm{s,y}}$, half tooth width $d_{\mathrm{s,t}}$, pole shoe tip width $d_{\mathrm{s,x}}$, yoke angle $\alpha_{\mathrm{s,y}}$, tooth angle $\alpha_{\mathrm{s,t}}$, and slot opening angle $\alpha_{\mathrm{s,v}}$. It is important to note, that these parameters defined the shape and the cross-section A_{slot} of the stator slots, in which concentrated windings were wound. The design of the stator's winding was further defined by

the number of turns in individual stator slots N_w and the diameter d_w of the applied wire. The assembled winding occupied a cross-section A_w within individual slots, where the remaining slot cross-section $A_{cool} = A_{slot} - A_w$ was exploited for inner air cooling of the machine, and is graphically presented in Fig. 1.

The design of the rotor cross-section was defined by the following geometric parameters: thickness of the air gap between the stator and the rotor d_{ag}, outer radius $r_{r,out} = r_{s,in} - d_{ag}$, inner radius, i.e., shaft radius r_{sh}, minimum thickness of the bridge, i.e., distance between air pockets and other surfaces of the rotor $d_{r,b}$, q-axis bridge width $d_{r,q}$, and the distance of the permanent magnet from the center of the rotor shaft $d_{r,y}$. Further, the permanent magnet was considered with a rectangular cross-section defined by A_{pm}. It is important to note that the shape and cross-section of the air pockets A_{ap} was defined by all other rotor parameters and is schematically presented in Fig. 1. The mechanical angle between the rotor and stator was θ, where the number of pole pairs p_p defined the electrical angle by $\theta_e = p_p\theta$.

Parametrically defined electromagnetic problems are typically addressed using State-of-the-Art FEM models. These models accurately account for nonlinear material properties and solve for the electromagnetic field distribution, theoretically allowing for the evaluation of various objective and constraint functions within an optimization process. However, while yielding precise results, this straightforward approach is computationally intensive and often impractical for iterative, optimization based, product design. Consequently, a primary objective of this research was to enhance the computational efficiency of MOO by substituting expensive models with suitable meta-models.

2.3. Definition of optimization objectives, key performance indicators and constraints

In order to adequately define the optimization problem, the optimization objectives, KPIs, and constraints must first be identified. This is in most cases an iterative process, where all three aspects are interconnected.

2.3.1. MOO objectives

In this paper, the objective of the MOO was to be able to select various optimal designs from the set of optimal solutions, i.e., the Pareto front, where two machine KPIs were considered simultaneously ($N_{\mathcal{F}} = 2$).

2.3.2. Key performance indicators

We selected the following two KPIs for the discussed mechatronic system:

1. m - total mass of the IPMSM, which considerably impacts the total mass of the handheld power tool, i.e., tool handling and comfort.
2. P_b - thermal stable base power, which impacts the maximum output power of the handheld power tool, i.e., tool capability and performance.

2.3.3. Constraints

Based on the discussed problem statement, the following constraints were identified:

(a) The outer dimensions of the IPMSM, i.e., the outer radius of the stator lamination stack $r_{s,out}$, and the length of the lamination stack l_s are prescribed.
(b) The mechanical subsystem of the drive remains unchanged, i.e., the bearings, the attached fan, and the diameter of the rotor shaft d_{sh} are fixed.
(c) The integration of the IPMSM into the pre-existing cooling subsystem maintains the original cooling power P_{cool}. The IPMSM utilizes internal cooling where the air is forced through the winding slots in the stator (exploiting A_{cool}) and across the air gap that separates the stator and rotor.
(d) The winding production process requires a prescribed slot shape and space for assembling the windings. The prescribed shape of the slot determines the values of the yoke angle $\alpha_{s,y}$, and the tooth angle $\alpha_{s,t}$. Further, the wire can be selected only from a discrete set of standard wire diameters $\boldsymbol{d}_{Cu}$, where the minimum and maximum wire diameters, $d_{Cu,min}$ and $d_{Cu,max}$, are defined by the winding technology. Winding technology is limited to concentrated windings.
(e) The existing fixed voltage of the battery and the operating speed range of the drive system predetermines a fixed number of turns of the stator windings N_w, a fixed number of pole pairs p_p and, consequently, a fixed number of stator slots.
(f) The production process of the stator and rotor stacks allows for modifications to the design of the machines's cross-section. Nevertheless, the manufacturing process requires adherence to certain fundamental parameters concerning the geometry of the cross-section. These are the air gap d_{ag}, and the minimum distance from the air pockets or magnets to the outer surface of the rotor $d_{r,b}$. Further, the properties of used electric steels are fixed, and the interior magnets can be placed only tangentially inside the rotor.

2.4. Definition of the MOO problem

Based on the presented MOO objectives, KPIs, and constraints, we defined a MOO scenario, which targeted the optimization of P_b and m. Furthermore, the presented KPIs and constraints enabled us to define the optimization search space, i.e., identify a set of optimization design variables $\boldsymbol{x}$ and their lower $\boldsymbol{x}_L$ and upper limits $\boldsymbol{x}_U$.

2.4.1. Optimization scenario

The goal was to increase the power density of the IPMSM by applying KPIs 1 and 2 within (2).

$$\begin{aligned} \min_{\boldsymbol{x}} \quad & \begin{cases} \mathcal{F}_P(\boldsymbol{x}) = -P_b(\boldsymbol{x}) \\ \mathcal{F}_m(\boldsymbol{x}) = m(\boldsymbol{x}) \end{cases} \\ \text{subject to} \quad & \mathcal{G}_A(\boldsymbol{x}) = \left(\frac{A_{cool}(\boldsymbol{x})}{A_{cool,ref}} - 1 \right) \leq 0.1 \\ & \boldsymbol{x}_L \leq \boldsymbol{x} \leq \boldsymbol{x}_U \end{aligned} \tag{2}$$

An inequality constraint function was applied, which was connected to the constraint (c) and prevented that the cooling cross-section A_{cool} of optimized designs increased more than 10% compared to the cooling cross-section of the reference design $A_{cool,ref}$. This deviation was determined based on a performed numerical thermal analysis, where it was estimated that a less than 10% deviation in the cooling cross-section does not significantly impact the cooling capacity of the existing cooling system. On the other hand, this deviation enabled adequate flexibility in realizing windings of various wire sizes from the prescribed discrete wire set.

2.4.2. Search space

The search space was identified based on the geometric parameters that were allowed to change and were related to the defined KPIs, as per Section 2.3. Eight rotor and stator iron core cross-section parameters were identified as design variables $\boldsymbol{x}$. The selected variables together with their upper and lower limits are presented in Table 1. All presented variables are normalized, where the length-based variables are scaled to the stator inner radius $r_{s,in}$ of the reference design, while the magnet cross-section A_{pm} is scaled by itself. A preliminary analysis, including the manufacturing constraints, informed the selection of the limits. This approach allowed for comprehensive adjustments across the entire feasible IPMSM geometry, which ensured a significant impact of $\boldsymbol{x}$ on the discussed KPIs.

The stator's inner radius $r_{s,in}$ was allowed to change in a range of 34.4% compared to the reference design. This allowed for significant

Table 1
Stator and rotor geometry optimization design variables with the prescribed lower and upper limits. All length-based variables are given in p.u. and are scaled to the stator inner radius $r_{s,in}$ of the reference design. The magnet cross-section is scaled to itself and is given in p.u., and the slot opening angle is in rad.

$\boldsymbol{x}$	Var.	Description	Ref.	$\boldsymbol{x}_U$	$\boldsymbol{x}_L$
x_1	$r_{s,in}$	Stator inner radius	1	1.241	0.896
x_2	$d_{r,q}$	q-axis bridge width	0.124	0.172	0.041
x_3	$d_{r,y}$	Magnet tip height	0.569	0.835	0.517
x_4	A_{pm}	Magnet cross-section	1	1.087	0.84
x_5	$d_{s,y}$	Yoke width	0.339	0.345	0.172
x_6	$d_{s,t}$	Half tooth width	0.189	0.345	0.172
x_7	$d_{s,x}$	Pole shoe tip width	0.081	0.214	0.069
x_8	$\alpha_{s,v}$	Slot opening angle	0.145	0.227	0.105

changes in the overall machine design. The rotor was defined by the q-axis bridge width $d_{r,q}$, magnet tip height $d_{r,y}$, and magnet cross-section A_{pm}. The lower limit of $d_{r,q}$ was set by manufacturing constraints, while the upper limit was chosen to allow flexibility in design. The limits of $d_{r,y}$ were closely linked to $r_{s,in}$, ensuring that different magnet positions could be accommodated within the rotor. The magnet cross-section A_{pm} was allowed to change in a range of 24.7%, allowing for significant changes in magnet size, favoring a design with a smaller magnet cross-section. The lower limit was defined by the minimum feasible size dictated by manufacturing constraints, while the upper limit was set to prevent unnecessary increases in magnet size due to the high cost of magnets. The remaining design variables defined the stator geometry. The yoke width $d_{s,y}$ and half tooth width $d_{s,t}$ shared the same upper and lower limits, allowing for significant modifications to the slot and, consequently, the winding layout. The lower limit of the yoke was determined by the minimum allowable mechanical constraints, ensuring structural integrity. The pole shoe tip width $d_{s,x}$ and slot opening angle $\alpha_{s,v}$ determined the pole shoe geometry. The limits of $\alpha_{s,v}$ were selected to cover the entire range of feasible angles, ensuring design flexibility. The lower bound of $d_{s,x}$ was set by manufacturing constraints, while the upper bound was selected to allow greater design flexibility.

The remaining parameters presented in Fig. 1 were fixed to the reference design values to comply with the discussed constraints in Section 2.3, and were thus regarded as fixed design parameters.

2.5. Models for the evaluation of KPIs

Within the optimization process, the defined KPIs 1 and 2 were evaluated based on corresponding objective functions $\mathcal{F}_P(\boldsymbol{x})$ and $\mathcal{F}_m(\boldsymbol{x})$, and the constraint function $\mathcal{G}_A(\boldsymbol{x})$. These have to adequately model the relationship between sets of design variables $\boldsymbol{x}$ and individual KPIs. Such KPI evaluations can be straightforward, and the corresponding objective functions can be easily expressed using simple analytic models. In the discussed case, the mass $\mathcal{F}_m(\boldsymbol{x})$, as well as the deviation of the cooling cross-section $\mathcal{G}_A(\boldsymbol{x})$ were directly evaluated based on design variables. However, in general, the evaluation of KPIs is complex and requires combining of several models. Such case was the evaluation of $\mathcal{F}_P(\boldsymbol{x})$, where the basis for evaluating are adequate FEM models that produce corresponding non-linear maps, which were further used in additional models to evaluate individual KPIs.

2.5.1. Limiting variations in cooling cross-section

The stator slot cross-section $A_{slot}(\boldsymbol{x})$ was directly determined by the geometry of the stator iron core's cross-section, i.e., the design variables $\boldsymbol{x}$ and the fixed parameters. In the individual designs, the slot cross-section was filled out with a wire from the discrete set $\boldsymbol{d}_{Cu}$ with such a diameter that the remaining part of the slot cross-sections (i.e., the cooling cross-section $A_{cool}(\boldsymbol{x})$) was not decreased compared to the reference cooling cross-section $A_{cool,ref}$. The wire diameter was determined by (3).

$$d_w(\boldsymbol{x}) = \max\left(\boldsymbol{d}_{Cu} \le \sqrt{\frac{4(A_{slot}(\boldsymbol{x}) - A_{cool,ref})}{N_w \pi}}\right) \tag{3}$$

This approach provided an equal or increased cooling cross-section A_{cool} compared to the reference cooling cross-section $A_{cool,ref}$. However, for specific designs, this approach allowed substantially larger A_{cool}, which would disrupt the balance within the thermal subsystem. To address this, the inequality constraint function $\mathcal{G}_A(\boldsymbol{x})$ was introduced by (4),

$$\mathcal{G}_A(\boldsymbol{x}) = \frac{A_{slot}(\boldsymbol{x}) - N_w \pi \left(\frac{d_w(\boldsymbol{x})}{2}\right)^2}{A_{cool,ref}} - 1 \tag{4}$$

which disregarded all the designs with more than 10% increase from the reference cooling cross-section $A_{cool,ref}$. Such a deviation was justified, as small changes of A_{cool} did not affect the cooling performance, as discussed in Section 2.4.1.

The constraint presented had a direct impact on the slot fill factor. With the cooling cross-section A_{cool} almost fixed and the slot cross-section A_{slot} varying, the amount of copper in the slots changed based on the automatically selected wire diameter d_w. Thicker wires corresponded to larger slot cross-sections, while thinner wires corresponded to smaller slot cross-sections. Consequently, the former increased the slot fill factor, whereas the latter decreased it. It is important to note that designs with increased power generally gravitated towards a higher fill factor, while designs with reduced mass typically resulted in a lower slot fill factor.

2.5.2. Evaluation of total mass

The objective function $\mathcal{F}_m(\boldsymbol{x})$ for evaluating the total mass of the individual IPMSM designs was constructed as a sum of the masses of the variable parts (i.e., all the parts that are dependent on the design variables $\boldsymbol{x}$) of the machine by (5),

$$\mathcal{F}_m(\boldsymbol{x}) = m_s(\boldsymbol{x}) + m_r(\boldsymbol{x}) + m_w(d_w(\boldsymbol{x}), \boldsymbol{x}) + m_{pm}(\boldsymbol{x}) \tag{5}$$

where m_s, m_r, m_w and m_{pm} are the total masses of the stator iron core, rotor iron core, coils of the stator windings and permanent magnets, respectively. Masses m_s, m_r and m_{pm} were directly calculated from respective volumes that were obtained by extruding cross-sections to the length l_s of the active part of the IPMSM and corresponding mass densities of materials. Further, when calculating the mass of the winding coils m_w, the selected wire diameter d_w and the mass of end-windings were considered.

2.5.3. Evaluation of thermally stable base output power

The objective function for evaluating the thermally stable base power P_b was defined by (6),

$$\mathcal{F}_P(\boldsymbol{x}) = -t_b(\boldsymbol{x})\omega_b(\boldsymbol{x}) \tag{6}$$

where t_b is the base torque and ω_b is the base mechanical speed. Base speed ω_b refers to the rated or nominal speed at which the IPMSM can produce its maximum power output (i.e., the base power P_b) in the so-called Maximum Torque Per Ampere (MTPA) operation, as presented in Fig. 2.

The base speed ω_b was determined based on the voltage-balance model in the amplitude-invariant dq reference frame given by (7),

$$\begin{bmatrix} u_d \\ u_q \end{bmatrix} = \begin{bmatrix} R(\boldsymbol{x}) & 0 \\ 0 & R(\boldsymbol{x}) \end{bmatrix} \begin{bmatrix} i_d \\ i_q \end{bmatrix} + \frac{d}{dt} \begin{bmatrix} \Psi_d(i_d, i_q, \boldsymbol{x}) \\ \Psi_q(i_d, i_q, \boldsymbol{x}) \end{bmatrix} + \omega p_p \begin{bmatrix} -\Psi_q(i_d, i_q, \boldsymbol{x}) \\ \Psi_d(i_d, i_q, \boldsymbol{x}) \end{bmatrix} \tag{7}$$

where $\boldsymbol{u}_{dq} = [u_d, u_q]^T$ is the vector of dq-frame voltages and $\boldsymbol{i}_{dq} = [i_d, i_q]^T$ is the vector of corresponding dq-frame currents. R is the phase

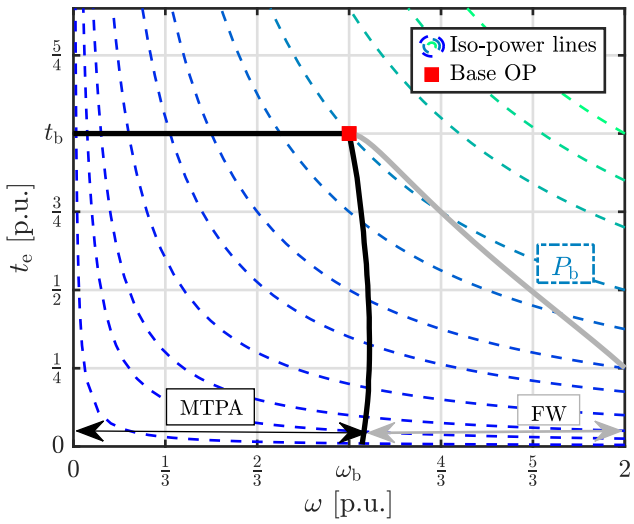

Fig. 2. Numerically FEM-based evaluated operation envelope of the reference IPMSM defined by the maximum thermally stable current $I_{s,max}$, with MTPA and Field Weakening (FW) region highlighted. The boundary between the MTPA and FW regions is marked by the line representing the maximum achievable speed at a given torque while operating in the MTPA OPs. The base OP is laying on the maximum isopower line in the MTPA region, which corresponds to the base power P_b.

resistance, which depends on the selected wire diameter d_w and IPMSM design defined by $\boldsymbol{x}$. The flux linkage in the q-axis Ψ_q is due to the current excitation of the stator windings, whereas the total flux linkage in the d-axis Ψ_d is due to the current excitation of the stator windings and due to the permanent magnet in the rotor. Both flux linkages are in general, significantly impacted by the OP of the IPMSM due to the saturation of the iron core. Therefore, they are expressed as nonlinear functions of currents i_d and i_q.

The base speed ω_b was calculated from (7) by applying adequate assumptions and simplifications (Morimoto et al., 1994; Dianov et al., 2022). In general, ω_b was evaluated by (8).

$$\omega_b(\boldsymbol{x}) = \frac{U_{dc} - R(\boldsymbol{x}) I_{s,max}(\boldsymbol{x})}{p_p \sqrt{\Psi^2_{d,b}(\boldsymbol{x}) + \Psi^2_{q,b}(\boldsymbol{x})}} \tag{8}$$

The base speed was defined by the maximum stator voltage that can be generated by the inverter (which is limited by the available DC-link voltage U_{dc}), the voltage drop due to maximum stator current $I_{s,max}$ ($I_{s,max}$ is limited due to thermal aspects) and by the flux linkages in d-axis $\Psi_{d,b}$ and in q-axis $\Psi_{q,b}$ in the observed OP. Flux linkages $\Psi_{d,b}$ and $\Psi_{q,b}$ are dependent on the design of the IPMSM, as well as on the magnetic excitation and saturation in the discussed OP. They can be determined based on the dq reference frame MTPA current components of $I_{s,max}$, i.e., $I_{d,b}(\boldsymbol{x})$ and $I_{q,b}(\boldsymbol{x})$, which are applied in the nonlinear functions $\Psi_q(I_{d,b}(\boldsymbol{x}), I_{q,b}(\boldsymbol{x}), \boldsymbol{x})$ and $\Psi_q(I_{d,b}(\boldsymbol{x}), I_{q,b}(\boldsymbol{x}), \boldsymbol{x})$.

The electromagnetic torque t_e is generated by the IPMSM due to the interaction between the flux linkages and stator currents and is in general defined by a nonlinear map (9),

$$t_e(i_d, i_q, \boldsymbol{x}) = \frac{3}{2} p_p \left(\Psi_d(i_d, i_q, \boldsymbol{x}) i_q - \Psi_q(i_d, i_q, \boldsymbol{x}) i_d \right) \tag{9}$$

where p_p is the number of pole pairs and the factor $\frac{3}{2}$ is due to the assumption of applying amplitude invariant transformations.

The base torque t_b corresponds to the maximum torque that IPMSMs can generate in steady state operation at ω_b, as presented in Fig. 2. It can be determined based on (9) by applying the current components $I_{d,b}$ and $I_{q,b}$, i.e., by (10).

$$t_b(\boldsymbol{x}) = t_e(I_{d,b}(\boldsymbol{x}), I_{q,b}(\boldsymbol{x}), \boldsymbol{x}) \tag{10}$$

The discussed base OP was different for individual IPMSM designs, therefore it was necessary to find the maximum thermally stable current $I_{s,max}$ and the corresponding MTPA-optimal combination of $I_{d,b}$ and $I_{d,q}$, for each design. The evaluation of $I_{s,max}$ for the reference design was performed using a validated multiphysics model, coupling the electromagnetic FEM model with a lumped-parameter thermal model (Garmut et al., 2024a). The value of $I_{s,max}$ was determined at a fixed end-winding temperature of 130 °C for the base OP. The thermally stable current $I_{s,max}$ depends on the cooling capacity of the cooling subsystem at ω_b. Based on a thermal sensitivity analysis, we determined that the variation of iron losses for feasible IPMSM designs within the defined search space was relatively low, because these designs operate at similar ω_b and at similar saturation levels, and the cooling subsystem was fixed (Constraint (c)). The variation in conduction losses in windings was, however, not negligible, because the design search space includes wires of various diameters. Based on the obtained results we assumed that the predominant component of losses that impacts the thermally stable current $I_{s,max}$ were the maximum allowable conduction losses $P_{Cu,max}$. These were determined based on the reference IPMSM design by evaluating iron core losses $P_{Fe,ref}$ at $\omega_{b,ref}$ and subtracting them from the cooling power $P_{cool,ref}$ in the discussed OP by (11).

$$P_{Cu,max} = P_{cool,ref} - P_{Fe,ref} \tag{11}$$

The thermally stable maximal phase current $I_{s,max}$ was consequently determined by (12).

$$I_{s,max}(\boldsymbol{x}) = \sqrt{\frac{2 P_{Cu,max}}{3 R(\boldsymbol{x})}} \tag{12}$$

Assuming that the nonlinear function of the electromagnetic torque $t_e(i_d, i_q)$ was known, the thermally stable base torque t_b was determined by finding the maximum torque within $t_e(i_d, i_q)$ that corresponds to the maximum thermally stable current $I_{s,max}$. Current combinations i_d and i_q can be alternatively expressed in polar coordinates by a current vector with amplitude $I_s^2 = i_d^2 + i_q^2$ and angle γ. In this way, the MTPA angle γ_b of $I_{s,max}$ for the base OP was determined by solving the nonlinear optimization problem given by (13).

$$\max_{\gamma} t_e(I_s, \gamma) \quad \text{s.t.} \quad I_s = I_{s,max} \tag{13}$$

Based on $I_{s,max}$ and the determined γ_b, both current components for $I_{d,b}$ and $I_{q,b}$ for generating t_b were obtained. Finally, t_b was calculated by (10).

The solution to (13) can be obtained analytically only when $t_e(i_d, i_q)$ is expressed as an adequate function (Dianov et al., 2022). It is important to note that the discussed IPMSM belongs to the group of highly non-linear machines, which is highlighted with the terms $\Psi_d(i_d, i_q)$, $\Psi_q(i_d, i_q)$, and $t_e(i_d, i_q)$ that are all highly dependent on the d-axis i_d and q-axis currents i_q, as presented in Fig. 3. These relationships cannot be obtained analytically, hence they are generally determined numerically in terms of adequate nonlinear maps by evaluating State-of-the-Art FEM models. Such FEM models connect the discussed relationships with the design variables $\boldsymbol{x}$ by leveraging numerical methods, where adequate FEM models evaluated in individual OPs defined by current combinations $I_{d,ev}$ and $I_{q,ev}$ can be regarded as intermediate models within the objective function.

3. FEM numerical models

3.1. Generation of intermediate data

An intermediate data value $y_{\bullet,j,k}$ ($\bullet$ is a placeholder denoting various electromagnetic quantities, e.g., t_e, Ψ_d, or Ψ_q) was generated based on a current-driven FEM model, where the model inputs were the stator current components $I_{d,ev,j}$ and $I_{q,ev,j}$ that define the evaluated OP j. It is important to note, that all the evaluated quantities were further

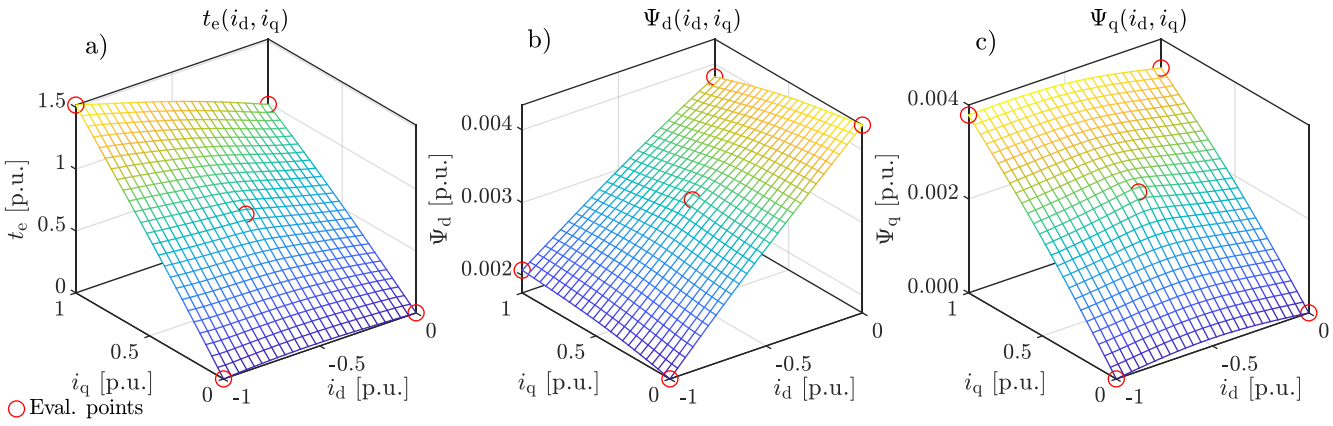

Fig. 3. Nonlinear maps calculated using RBF interpolation on 5 simulated points of: (a) the torque t_e, (b) magnetic flux in d-axis Ψ_d and (c) magnetic flux in q-axis Ψ_q.

dependent on the position k of the rotor in respect to the stator, i.e., on the angle θ (presented in Fig. 1). Consequently, all OPs were evaluated for N_θ uniformly distributed evaluation angles $\boldsymbol{\theta}_{ev} = \left[\theta_{ev,1}, \dots, \theta_{ev,N_\theta}\right]$ within one electrical period. The data dependency on θ was not significant for the evaluation of the objective function $\mathcal{F}_P(\boldsymbol{x})$ (6), as it affected parameters such as torque ripple, but did not impact the average torque values t_e, nor the base speed ω_b. These variables depended only on the average values in respect to θ, as defined by (8) and (9), respectively. The average value in OP j over the evaluated angles was defined by (14),

$$\overline{y}_{\bullet,j}(\boldsymbol{x}) = \frac{1}{N_\theta}\sum_{k=1}^{N_\theta} \mathcal{M}_{FEM}(I_{d,ev,j}, I_{q,ev,j}, \theta_{ev,k}, \boldsymbol{x}) \tag{14}$$

where $k = 1, \dots, N_\theta$. Further, by evaluating N_{OP} OPs, which were determined by the current component combination from the current evaluation vectors $\boldsymbol{I}_{d,ev} = \left[I_{d,ev,1}, \dots, I_{d,ev,N_{OP}}\right]$ and $\boldsymbol{I}_{q,ev} = \left[I_{q,ev,1}, \dots, I_{q,ev,N_{OP}}\right]$, the resulting average values were organized into data vectors $\overline{\boldsymbol{y}}_\bullet(\boldsymbol{x})$ defined by (15).

$$\overline{\boldsymbol{y}}_\bullet(\boldsymbol{x}) = \left[\overline{y}_{\bullet,1}(\boldsymbol{x}), \dots, \overline{y}_{\bullet,N_{OP}}(\boldsymbol{x})\right]^{1\times N_{OP}} \tag{15}$$

3.2. FEM advantages and limitations

The advantage of FEM models was that they enable the evaluation of several intermediate variables $y_{\bullet,j,k}$ with a single FEM evaluation. In this way all the data for FEM-based numerical approximation of t_e, Ψ_d, Ψ_q were obtained simultaneously by numerical evaluation of individual OPs of interest, where adequate $\boldsymbol{\theta}_{ev}$ were considered. The FEM-based evaluations for different OPs and rotor positions were independent; therefore, parallel computing can be employed. The main challenge was, however, that the current components $I_{d,b}(\boldsymbol{x})$ and $I_{q,b}(\boldsymbol{x})$ in the selected OPs required for evaluation of objective function (6) depended on the design variables $\boldsymbol{x}$ and were not known *a priori*. To determine these current components, numerical methods must be applied, which in general necessitate an evaluation of discussed FEM models in hundreds of OPs (i.e., $j = 1, \dots, N_{OP}$) and for multiple rotor positions (i.e., $k = 1, \dots, N_\theta$) to either gather enough numerical data points for approximation of $t_e(i_d, i_q)$, $\Psi_d(i_d, i_q)$, and $\Psi_q(i_d, i_q)$ or for iterative determination of the discussed components. Thus, integrating these models directly into optimization for engineering applications was impractical because FEM models were computationally intensive to evaluate, even at a single OP.

3.3. Approximation of nonlinear maps

The determination of $I_{d,b}(\boldsymbol{x})$ and $I_{q,b}(\boldsymbol{x})$ was based on (13), where both components for the base OPs were determined from the nonlinear map $t_e(i_d, i_q)$. Besides $t_e(i_d, i_q)$, also $\Psi_d(i_d, i_q)$ and $\Psi_q(i_d, i_q)$ were adequately numerically approximated based on the FEM models by interpolation between the data points. The simplest numerical interpolation is the bilinear interpolation, however, in this case, hundreds of OPs still need to be evaluated at each optimization step to approximate the discussed maps for each specific design. This was significantly reduced if these maps were approximated based on an interpolation method that required a reduced number of FEM-evaluated OPs. The numerically approximated maps $\tilde{z}_\bullet(i_d, i_q)$ (i.e., $\tilde{z}_\bullet$ is a generalized expression for the three evaluated maps $\tilde{t}_e(i_d, i_q)$, $\tilde{\Psi}_d(i_d, i_q)$ and $\tilde{\Psi}_q(i_d, i_q)$) were obtained by performing a multi-quadric Radial Basis Function (RBF) interpolation (Buhmann, 2003) by (16),

$$\tilde{z}_\bullet(i_d, i_q, \boldsymbol{x}) = \mathcal{M}_{RBF}(\overline{\boldsymbol{y}}_\bullet(\boldsymbol{x}), \boldsymbol{I}_{d,ev}, \boldsymbol{I}_{q,ev}) \tag{16}$$

where as low as five OPs (i.e., $N_{OP} = 5$) were required for interpolation. For adequate results, the OPs must be selected strategically, as presented in Fig. 3. Such a simplification heavily reduced the computation intensity and required time in each optimization step, but introduced a slight deviation in obtained maps.

3.4. Computationally efficient FEM-based models

To reduce the extensive simulation durations, a Computationally Efficient Finite Element Method (CE-FEM) numerical evaluation was applied. CE-FEM models aim to reduce computational complexity and time while maintaining accuracy, making them particularly useful in optimization processes where numerous evaluations are required. The CE-FEM approach is in detail discussed in Sizov et al. (2012) and Garmut et al. (2022). The basis was a parametrized FEM model, corresponding to the discussion in Section 2.2, where the parameters of the model included all the design variables $\boldsymbol{x}$ from the defined optimization search space (presented in Section 2.4.2).

The computational efficiency was significantly reduced with a series of assumptions that enable significantly reduced modeled geometry of the IPMSM as well as required rotor positions (Sizov et al., 2012). In this way, only 5 rotor positions (i.e., $N_\theta = 5$) in 1/6 of an electric period were required to evaluate the whole electric period for every dq-current combination. The results were obtained on 1/2 of the full FEM model geometry, where the symmetry of the discussed 4-pole IPMSM was exploited. The complete period was subsequently reconstructed, where the missing values were determined using the fast Fourier transform, a transformation in the dq reference frame, and averaging the obtained values to evaluate the magnetic flux linkages in d-axis and q-axis, and the torque. By evaluating an adequate array of OPs and applying RBF interpolation, nonlinear maps $\tilde{\Psi}_d(i_d, i_q)$, $\tilde{\Psi}_q(i_d, i_q)$, and $\tilde{t}_e(i_d, i_q)$ were generated.

4. Meta-models

Performing MOO with the presented CE-FEM based interpolated maps is still computationally expensive. Computation efficiency was thus greatly improved by replacing all CE-FEM model functions with adequate meta-models. Meta-models provide a higher level of abstraction and significantly reduce complexity while maintaining accuracy.

4.1. ANNs replacing FEM-based numerical models

The meta-model used to replace the FEM-based numerical evaluations was a regression feedforward neural network, tailored for function fitting and regression (Li et al., 2021; Khan et al., 2020b; Al-Majidi et al., 2020). Separate ANNs were used to model single output values $\tilde{y}_{\bullet,j}$ in a selected OP j for a given set of design variables $\boldsymbol{x}$. Multiple Multiple-Input Single-Output (MISO) ANNs were used to predict individual outputs $\tilde{y}_{\bullet,j}$. This approach improves accuracy with a smaller dataset, as each ANN is dedicated to learning the specific relationship between the input parameters $\boldsymbol{x}$ and a single output $\tilde{y}_{\bullet,j}$, reducing model complexity and improving generalization. This necessitated training multiple ANNs for different types of outputs and OPs with the same design variable dataset.

Selecting the appropriate data that would be replaced by the meta-models was crucial. For instance, training ANNs to predict intermediate data $y_{\bullet,j,k}(\boldsymbol{x})$ would result in an impractically high number of meta-models. Conversely, training ANNs to directly predict KPIs $\mathcal{F}_{\mathrm{P}}(\boldsymbol{x})$ from (6) would significantly reduce the accuracy of the meta-models. To avoid both extremes, the ANNs were used to predict the intermediate averaged FEM output values $\overline{y}_{\bullet,j}$ given by (14).

The predicted intermediate output values $\tilde{y}_{\bullet,j}$ were thus provided by ANNs by (17),

$$\tilde{y}_{\bullet,j}(\boldsymbol{x}) = \mathcal{N}_{\mathrm{ANN},\bullet,j}(\boldsymbol{x}) \tag{17}$$

where $\tilde{y}_{\bullet,j}$ slightly differs from $\overline{y}_{\bullet,j}$, depending on the accuracy of the ANN. Further, the outputs of individual ANNs were combined into a data vector $\tilde{\boldsymbol{y}}_{\bullet}(\boldsymbol{x})$ by (18),

$$\tilde{\boldsymbol{y}}_{\bullet}(\boldsymbol{x}) = \left[\tilde{y}_{\bullet,1}(\boldsymbol{x}), \dots, \tilde{y}_{\bullet,N_{\mathrm{OP}}}(\boldsymbol{x})\right]^{1\times N_{\mathrm{OP}}} \tag{18}$$

analogously to (15). By inserting $\tilde{\boldsymbol{y}}_{\bullet}$ into (16), nonlinear maps $\tilde{\Psi}_{\mathrm{d}}(i_{\mathrm{d}}, i_{\mathrm{q}})$, $\tilde{\Psi}_{\mathrm{q}}(i_{\mathrm{d}}, i_{\mathrm{q}})$, and $\tilde{\imath}_{\mathrm{e}}(i_{\mathrm{d}}, i_{\mathrm{q}})$ were generated and the objective function $\mathcal{F}_{\mathrm{P}}(\boldsymbol{x})$ was evaluated, as outlined in Section 2.5.

4.2. Dataset generation

To obtain accurate meta-models (i.e., ANNs), a sufficient amount of data was required. Latin Hypercube Sampling (LHS) was employed to generate N_{d} design variables vectors $\boldsymbol{x}_m$, where $m = 1, \dots, N_{\mathrm{d}}$. All $\boldsymbol{x}_m$ were combined in to a design variable matrix $\boldsymbol{X}$, defined by (19),

$$\boldsymbol{X}^{N_{\mathrm{d}}\times N_{\mathrm{x}}} = \mathcal{M}_{\mathrm{LHS}}(\boldsymbol{x}_{\mathrm{L}}, \boldsymbol{x}_{\mathrm{U}}, N_{\mathrm{d}}) = \left[\boldsymbol{x}_1, \dots, \boldsymbol{x}_{N_{\mathrm{d}}}\right]^{\mathrm{T}} \tag{19}$$

where the upper $\boldsymbol{x}_{\mathrm{U}}$ and lower limits $\boldsymbol{x}_{\mathrm{L}}$ of the design variable limited the search space. The size of the design variables matrix $\boldsymbol{X}$ was the size of the sample set N_{d} times the number of design variables N_{x}.

For every design variable vector $\boldsymbol{x}_m$ a corresponding intermediate data vector $\overline{\boldsymbol{y}}_{\bullet,m} = \left[\overline{y}_{\bullet,m,1}, \dots, \overline{y}_{\bullet,m,N_{\mathrm{OP}}}\right]^{1\times N_{\mathrm{OP}}}$ containing solutions for all OPs was evaluated by (14) and (15). By combining the intermediate data vectors $\overline{\boldsymbol{y}}_{\bullet,m}$ for all N_{d} design variable vectors $\boldsymbol{x}_m$, we obtained a matrix, defined by (20),

$$\begin{aligned}\overline{\boldsymbol{Y}}_{\bullet} &= \begin{bmatrix} \overline{y}_{\bullet,1,1}(\boldsymbol{x}_1) & \cdots & \overline{y}_{\bullet,1,N_{\mathrm{OP}}}(\boldsymbol{x}_1) \\ \vdots & \ddots & \vdots \\ \overline{y}_{\bullet,N_{\mathrm{d}},1}(\boldsymbol{x}_{N_{\mathrm{d}}}) & \cdots & \overline{y}_{\bullet,N_{\mathrm{d}},N_{\mathrm{OP}}}(\boldsymbol{x}_{N_{\mathrm{d}}}) \end{bmatrix}^{N_{\mathrm{d}}\times N_{\mathrm{OP}}} \\ &= \begin{bmatrix} \overline{\boldsymbol{y}}_{\bullet,1}^{N_{\mathrm{d}}\times 1} & \cdots & \overline{\boldsymbol{y}}_{\bullet,N_{\mathrm{OP}}}^{N_{\mathrm{d}}\times 1} \end{bmatrix}^{N_{\mathrm{d}}\times N_{\mathrm{OP}}}\end{aligned} \tag{20}$$

where the rows were the intermediate data vectors $\overline{\boldsymbol{y}}_{\bullet,m}^{1\times N_{\mathrm{OP}}}$ containing the data for all OPs and one design variable vector $\boldsymbol{x}_m$, and the columns were the intermediate solution data vectors $\overline{\boldsymbol{y}}_{\bullet,j}^{N_{\mathrm{d}}\times 1}$ that correspond to the design variable matrix $\boldsymbol{X}$ and contain all solutions for one OP .

Every ANN $\mathcal{N}_{\mathrm{ANN},\bullet,j}$ was modeled using the design variable matrix $\boldsymbol{X}$ and an intermediate solution vector $\overline{\boldsymbol{y}}_{\bullet,j}$ containing data for one OP. The ANN training was defined by (21),

$$\mathcal{N}_{\mathrm{ANN},\bullet,j} = \mathcal{M}_{\mathrm{ANN}}(\overline{\boldsymbol{y}}_{\bullet,j}, \boldsymbol{X}) \tag{21}$$

where $\mathcal{M}_{\mathrm{ANN}}$ presents the ANN training function. This resulted in ANNs that provided $\tilde{y}_{\bullet,j}$ by (17) for all three electromagnetic quantities t_{e}, Ψ_{d}, or Ψ_{q} across N_{OP} evaluated OPs.

5. Implementation and evaluation of models within MOO

To obtain the Pareto front, the presented objective functions $\mathcal{F}_{\mathrm{P}}(\boldsymbol{x})$ and $\mathcal{F}_{\mathrm{m}}(\boldsymbol{x})$ and the constraint function $\mathcal{G}_{\mathrm{A}}(\boldsymbol{x})$ had to be evaluated and implemented in a MOO algorithm.

5.1. Objective and constraint functions

The objective function $\mathcal{F}_{\mathrm{m}}(\boldsymbol{x})$ for evaluating the total mass and the constraint function $\mathcal{G}_{\mathrm{A}}(\boldsymbol{x})$ to limit the deviation of the cooling cross-section were calculated directly by using analytical models (i.e., (3) to (5)), which were evaluated based on the design variables $\boldsymbol{x}$. The models presented in Sections 2.5.1 and 2.5.2 were implemented using Matlab functions, which were directly used in the MOO.

The evaluation of the objective function $\mathcal{F}_{\mathrm{P}}(\boldsymbol{x})$ was initially based on an adequate FEM model, significantly increasing computation time. To obtain $\mathcal{F}_{\mathrm{P}}$ the evaluation process was split into two parts, as presented in Fig. 4. The first was the FEM-based numerical evaluation, where the intermediate data $\overline{\boldsymbol{y}}_{\bullet}$ was generated, as presented in Fig. 4(a).

In the second part, the numerical and analytical OP evaluation of $\mathcal{F}_{\mathrm{P}}$ followed, as presented in Fig. 4(c) and (d), based on the obtained maps, thermally stable maximal phase current, DC voltage, and phase resistance. The process was implemented using Matlab, except for the current driven CE-FEM, given by (14), which was modeled using Ansys Maxwell 2D and Matlab, as presented in Section 3.4. The nonlinear maps were obtained by interpolation of OP intermediate data in five OPs with a multi-quadric RBF interpolation in Matlab, provided by Wiens (2024).

To avoid the time-consuming FEM-based numerical evaluation required to evaluate $\mathcal{F}_{\mathrm{P}}$ for each set of design variables $\boldsymbol{x}$ in the MOO, it was replaced with suitable ANNs, trained using Matlab's feedforward ANNs (MathWorks, 2024a). The ANNs predicted intermediate data $\tilde{\boldsymbol{y}}_{\bullet}$, as presented in Fig. 4(b), which directly replaced the FEM-based numerical intermediate data evaluation. In addition to ANN models, a Kriging model was employed to predict intermediate data and evaluate the performance of ANNs against State-of-the-Art meta-models used in electric machine optimization (Sun et al., 2021; Li et al., 2021). The Kriging model, which utilizes Gaussian Process Regression (GPR), was trained using the squared exponential kernel function. This model is part of Matlab's Statistics and Machine Learning Toolbox (MathWorks, 2025).

5.2. Data collection and ANN training

To train the ANNs, adequate data was collected, as shown in Fig. 5 and Section 4.2. To ensure accurate ANNs, the number of samples N_{d} was set to 1500 based on a preliminary analysis, which demonstrated that this sample size offers a good balance between accuracy and computational efficiency. The obtained results further confirm that the determined sample size enabled accurate predictions. The training process employed the CE-FEM model used in intermediate data evaluation, with the exception that the intermediate data was not directly evaluated, but was instead saved for every set of design variables.

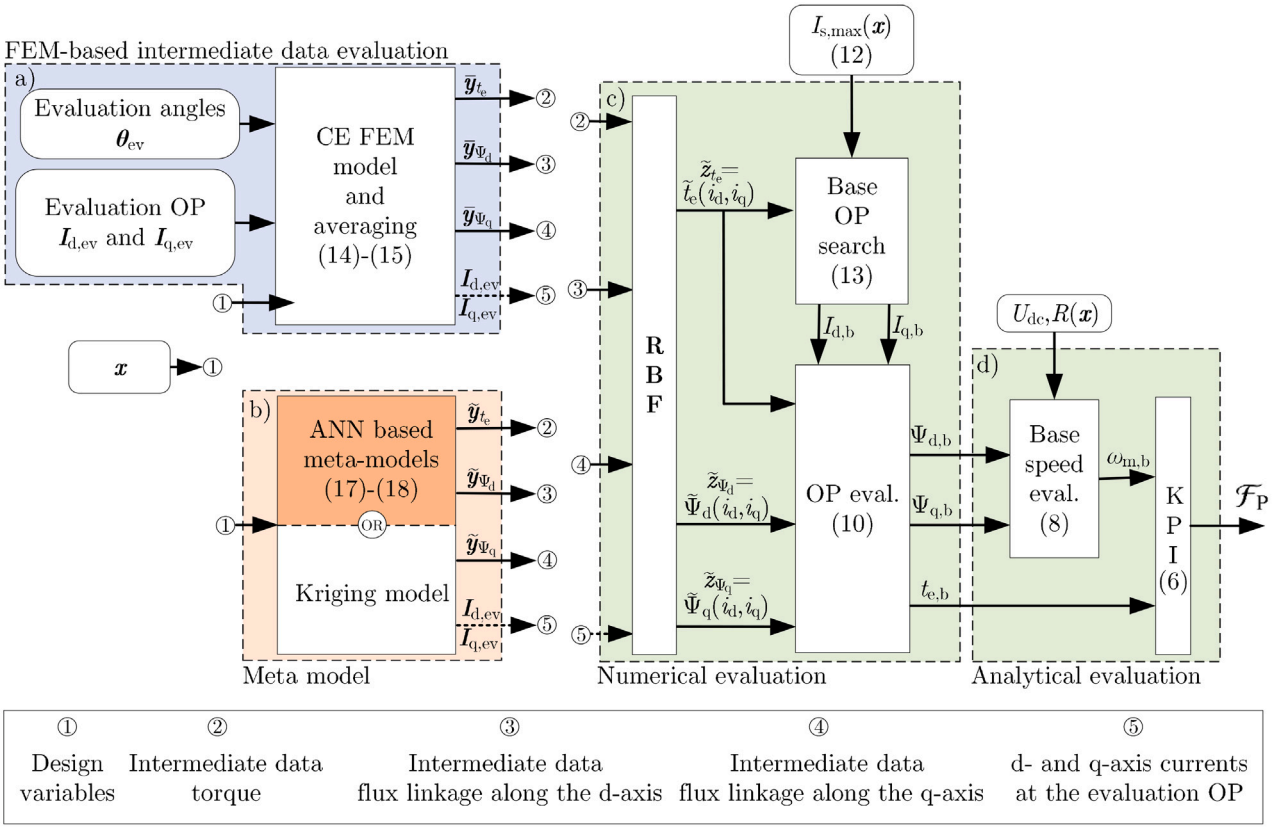

Fig. 4. Shematic presentation for evaluation of the objective function $\mathcal{F}_P(x)$: (a) FEM-based intermediate data evaluation, (b) meta-model based intermediate data evaluation, (c) numerical OP evaluation and (d) analytical objective function evaluation. The ANN-based meta-model approach is highlighted, as it was central in performing the presented MOO.

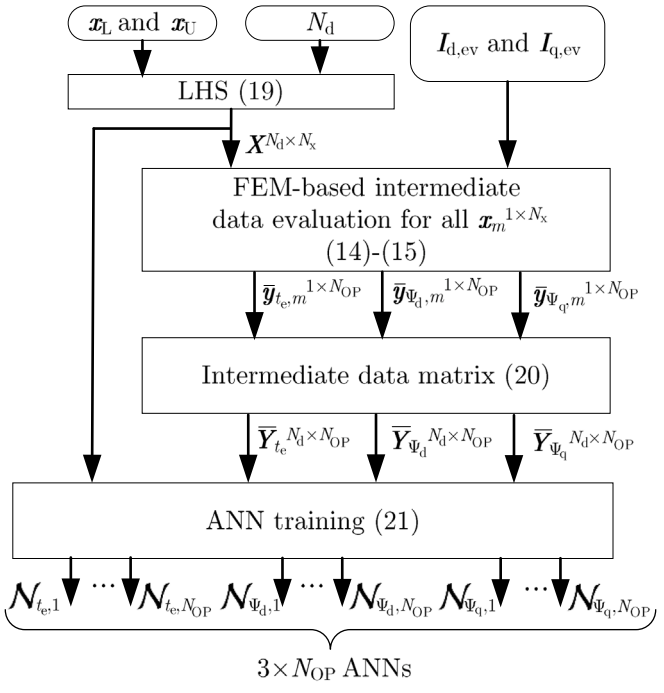

Fig. 5. Schematic representation for generating the intermediate data that are used for training the ANNs.

Identical ANN architectures were used for all data outputs, as a preliminary study showed no significant improvement in accuracy when different architectures were employed. Each MISO ANN consisted of an input layer with N_x neurons, three hidden layers with 20, 30, and 10 neurons, respectively, and an output layer with a single neuron.

The ANNs were trained using the Levenberg–Marquardt optimization algorithm, and the performance was evaluated with the Mean Squared Error (MSE). The dataset was normalized using min–max normalization and then split into 70% training, 15% validation, and 15% testing data. During ANN model training, the training data adjusted the ANN's parameters, while the validation data monitored performance and prevented overfitting. Finally, the test data evaluated how well the model performed on unseen data.

The training and validation data from the ANN training process were used for the Kriging model formulation, while the test data were utilized to assess the model's generalization ability.

5.3. Implementation of MOO

A two-objective optimization with one inequality constraint, defined by (2) was performed with Matlab's multi-objective genetic algorithm, which is an elitist genetic algorithm, a variant of NSGA-II (Li et al., 2023; MathWorks, 2024b). The maximal number of iterations was set to 300, and the population size per generation was set to 100.

The Hypervolume Indicator (HI) was used as a performance assessment metric of the MOO. HI assesses the volume of the objective space dominated by the Pareto front relative to a predefined reference point. It evaluates both convergence and diversity, with higher values indicating better optimization results (Beume et al., 2009; Shang et al., 2021).

5.4. Evaluation of time-reduction measures

To assess the increase in computational efficiency achieved by employing different time-reduction measures (i.e., CE-FEM, RBF, ANNs,

Table 2
Comparison of computation times and total number of FEM evaluations for optimization Approaches 1 to 4. The presented values correspond to MOO with $N_{\mathrm{MOO}} = 30\,000$ cost function evaluations. ▲ serves as a placeholder, representing either FEM, ANN+data or ANN and ▼ serves as a placeholder, representing either MOO or data.

Appr.	N_{d}	N_{OP}	N_{θ}	$N_{\mathrm{FEM},\blacktriangledown}$	t_{FEM} [s]	t_{train} [s]	t_{cal} [s]	t_{ANN} [s]	t_{opt} [s]	$t_{\Sigma,\blacktriangle}$ [s]
1	/	100	360	$1.08 \cdot 10^{9}$	4	/	0.03	/	0.24	$4.32 \cdot 10^{9} \approx 137$ years
2	/	5	5	$7.50 \cdot 10^{5}$	3.4	/	0.03	/	0.24	$2.56 \cdot 10^{9} \approx 29.6$ days
3	1500	5	5	$3.75 \cdot 10^{4}$	3.4	15	0.03	$0.5 \cdot 10^{-4}$	0.24	$1.36 \cdot 10^{5} \approx 1.57$ days
4	/	/	/	/	/	/	0.03	$0.5 \cdot 10^{-4}$	0.24	$8.10 \cdot 10^{3} \approx 2.25$ h

. . .) within the MOO, two metrics were introduced that evaluated both the total computation time and the total number of FEM evaluations.

These metrics were evaluated for four MOO approaches to assess the impact of various time-reduction techniques on computational efficiency. A direct FEM-based MOO without any time reduction measures was considered in Approach 1. Approach 2 was also a direct FEM-based MOO but considered time-reduction techniques such as CE-FEM and RBF. Approach 2 was comprised of sub-evaluations that are presented in Fig. 4(a), (c), and (d). Approach 3 further enhanced computational efficiency by implementing ANN-based meta-models. The training data was generated by using the sub-evaluation in Fig. 4(a), while the design evaluation within the MOO was performed by sub-evaluations presented in Fig. 4(b), (c), and (d). Approach 4 considered repeating MOO by reusing the pre-trained ANN-based meta-models from Approach 3. In Approach 4, only the MOO process was analyzed, where the corresponding design sub-evaluations are presented in Fig. 4(b), (c), and (d).

A single magnetostatic FEM evaluation provided simultaneously three numerical values (i.e., $y_{\bullet,j,k}$) as described by (14). The required simulation time for a single evaluation of FEM models was denoted by t_{FEM}. It is important to note that by exploiting the symmetry of the machine's geometry, t_{FEM} was reduced in comparison to evaluation of the full FEM model. Regardless, to fully characterize a machine's design in a given OP, the entire electrical period must be evaluated at a minimum of $N_{\theta} = 360$ angle positions. This number was significantly reduced by using the CE-FEM model, which is discussed in Section 3.4 and corresponds to the sub-evaluation presented in Fig. 4(a). The CE-FEM model required only $N_{\theta} = 5$ angle positions per OP. Further, generating the full nonlinear maps for $t_{\mathrm{e}}(i_{\mathrm{d}}, i_{\mathrm{q}})$, $\Psi_{\mathrm{d}}(i_{\mathrm{d}}, i_{\mathrm{q}})$, and $\Psi_{\mathrm{q}}(i_{\mathrm{d}}, i_{\mathrm{q}})$ typically requires evaluating at least $N_{\mathrm{OP}} = 100$ OPs to enable bilinear interpolation and obtain $I_{\mathrm{d,b}}$ and $I_{\mathrm{q,b}}$ by using (13). By employing RBF as described in (16), the required number of OP evaluations was reduced to $N_{\mathrm{OP}} = 5$.

Within the MOO process, the objective functions $\mathcal{F}_{\mathrm{P}}$ and $\mathcal{F}_{\mathrm{m}}$, and the constraint function $\mathcal{G}_{\mathrm{A}}$ were evaluated a total of N_{MOO} times. The total number of FEM evaluations $N_{\mathrm{FEM,MOO}}$ in the direct FEM-based MOO is defined by (22),

$$N_{\mathrm{FEM,MOO}} = N_{\mathrm{MOO}} N_{\mathrm{OP}} N_{\theta} \tag{22}$$

where N_{OP} and N_{θ} can be determined for the full FEM model or for the CE-FEM model. Notably, by applying CE-FEM and RBF interpolation, $N_{\mathrm{FEM,MOO}}$ was reduced by a factor of 1440.

The evaluation of $\mathcal{F}_{\mathrm{P}}$ required FEM models, while $\mathcal{F}_{\mathrm{m}}$ and $\mathcal{G}_{\mathrm{A}}$ were computed analytically. The numerical and analytical evaluations of the intermediate data are presented in Fig. 4(c) and (d), respectively. These sub-evaluations were performed in t_{cal} for individual machine design, where t_{cal} also included evaluation of $\mathcal{F}_{\mathrm{m}}$ and $\mathcal{G}_{\mathrm{A}}$. Finally, the MOO algorithm required $N_{\mathrm{MOO}} \cdot t_{\mathrm{opt}}$ to compute the Pareto front, excluding cost function evaluations, with a per-design optimization evaluation time of t_{opt}.

The total computation time $t_{\Sigma,\mathrm{FEM}}$ required to obtain the Pareto front by using direct FEM-based optimization was, thus, defined by (23).

$$\begin{aligned} t_{\Sigma,\mathrm{FEM}} &= N_{\mathrm{MOO}}(N_{\mathrm{OP}} N_{\theta} t_{\mathrm{FEM}} + t_{\mathrm{cal}} + t_{\mathrm{opt}}) \\ &= N_{\mathrm{FEM,MOO}} t_{\mathrm{FEM}} + N_{\mathrm{MOO}}(t_{\mathrm{cal}} + t_{\mathrm{opt}}) \end{aligned} \tag{23}$$

Ultimately, ANNs were introduced to replace the FEM evaluations in the MOO, i.e., the FEM-based sub-evaluation in Fig. 4(a) was replaced by the ANN-based sub-evaluation in Fig. 4(b). To train the ANNs, N_{d} CE-FEM-based intermediate data evaluations were performed to obtain the full dataset, which resulted in the total number of FEM evaluations $N_{\mathrm{FEM,data}}$ defined by (24).

$$N_{\mathrm{FEM,data}} = N_{\mathrm{d}} N_{\mathrm{OP}} N_{\theta} \tag{24}$$

The corresponding total data collection time $t_{\Sigma,\mathrm{data}}$ was defined by (25).

$$t_{\Sigma,\mathrm{data}} = N_{\mathrm{FEM,data}} t_{\mathrm{FEM}} \tag{25}$$

This dataset was generated using a CE-FEM model (corresponding to Fig. 4(a)) in five OPs required for the RBF interpolation (i.e., $N_{\mathrm{OP}} = 5$, $N_{\theta} = 5$). After gathering the data, the training of the individual ANN required t_{train}. In total $3N_{\mathrm{OP}}$ ANNs were trained (because MISO ANNs were applied for modeling of three variables, as presented in Fig. 5), which resulted in the total ANN training time $t_{\Sigma,\mathrm{train}}$ defined by (26).

$$t_{\Sigma,\mathrm{train}} = 3 N_{\mathrm{OP}} t_{\mathrm{train}} \tag{26}$$

The total time required for evaluating the Pareto front $t_{\Sigma,\mathrm{ANN}}$ with the trained ANNs is defined by (27),

$$t_{\Sigma,\mathrm{ANN}} = N_{\mathrm{MOO}}(t_{\mathrm{cal}} + t_{\mathrm{ANN}} + t_{\mathrm{opt}}) \tag{27}$$

where t_{cal} corresponds to the sub-evaluations in Fig. 4(c) and (d) and t_{ANN} corresponds to the sub-evaluations in Fig. 4(b). Finally, the total time required to evaluate the Pareto front $t_{\Sigma,\mathrm{ANN+data}}$, including data collection and ANN training is defined by (28).

$$t_{\Sigma,\mathrm{ANN+data}} = t_{\Sigma,\mathrm{data}} + t_{\Sigma,\mathrm{train}} + t_{\Sigma,\mathrm{ANN}} \tag{28}$$

6. Results

6.1. Computational efficiency

The computation time and total number of FEM evaluations were evaluated for Approaches 1 to 4, which are defined in Section 5.4. All evaluations were performed on a standard desktop computer equipped with an Intel Xeon W-2235 CPU, NVIDIA Quadro P2200 GPU, 64 GB DDR4 RAM, and a 1.5 TB SSD running Windows 11 Pro.

The total number of design evaluations in the MOO was $N_{\mathrm{MOO}} = 30000$, and the training dataset size was $N_{\mathrm{d}} = 1500$. The corresponding evaluation times required for the different sub-evaluations within the analyzed approaches are presented in Table 2. Table 2 also summarizes the total FEM evaluations and overall computation time for all four MOO Approaches, highlighting the impact of the applied time-reduction strategies.

Overall, it was observed that the ANN evaluation time t_{ANN} was significantly lower than the calculation time t_{cal}, indicating that the ANN's contribution to the total evaluation time $t_{\Sigma,\blacktriangle}$ during the MOO was negligible.

In Approach 1 (i.e., without any time reduction measures and a direct optimization approach) the total computation time was approximated to $t_{\Sigma,\mathrm{FEM}} \approx 137$ years (equivalent to $N_{\mathrm{FEM,MOO}} = 1.08 \cdot 10^{9}$

Table 3
Computation times and total number of FEM evaluations for ANN-based optimization (Approach 3), broken down into data collection $t_{\Sigma,\text{data}}$, training $t_{\Sigma,\text{train}}$, and optimization $t_{\Sigma,\text{ANN}}$. The presented values correspond to MOO with 30 000 cost function evaluations.

Data collection						ANN training		MOO				
N_d	N_OP	N_θ	$N_\text{FEM,data}$	t_FEM [s]	$t_{\Sigma,\text{data}}$ [s]	t_train [s]	$t_{\Sigma,\text{train}}$ [s]	N_MOO	t_cal [s]	t_ANN [s]	t_opt [s]	$t_{\Sigma,\text{ANN}}$ [s]
1500	5	5	$3.75 \cdot 10^4$	3.4	$1.28 \cdot 10^5$	15	225	30 000	0.03	$0.5 \cdot 10^{-4}$	0.24	$8.10 \cdot 10^3$

Table 4
Comparison of MSE values for various Kriging and ANN models. MSE values for different Kriging models, where model formulation is performed using both training and validation data. The test data MSE values indicate the generalization performance of the models. The total MSE for the ANN model training phase includes both training and validation data. The final column lists the number of epochs used for training each model.

	Kriging MSE		ANNs MSE			MSE	
	Model formulation		ANN model training				
$\tilde{y}_{\bullet,j}$		Test data	Training data	Validation data	Total	Test data	Epochs
$\tilde{y}_{\Psi_\text{d},1}$	$5.177 \cdot 10^{-6}$	$2.991 \cdot 10^{-5}$	$1.095 \cdot 10^{-6}$	$3.106 \cdot 10^{-6}$	$1.450 \cdot 10^{-6}$	$5.674 \cdot 10^{-6}$	152
$\tilde{y}_{\Psi_\text{d},2}$	$5.901 \cdot 10^{-6}$	$3.346 \cdot 10^{-5}$	$2.654 \cdot 10^{-6}$	$1.190 \cdot 10^{-5}$	$4.286 \cdot 10^{-6}$	$1.154 \cdot 10^{-5}$	40
$\tilde{y}_{\Psi_\text{d},3}$	$6.260 \cdot 10^{-6}$	$4.196 \cdot 10^{-5}$	$1.333 \cdot 10^{-6}$	$5.617 \cdot 10^{-6}$	$2.089 \cdot 10^{-6}$	$6.793 \cdot 10^{-6}$	145
$\tilde{y}_{\Psi_\text{d},4}$	$6.316 \cdot 10^{-6}$	$2.463 \cdot 10^{-5}$	$1.439 \cdot 10^{-6}$	$7.174 \cdot 10^{-6}$	$2.451 \cdot 10^{-6}$	$7.442 \cdot 10^{-6}$	78
$\tilde{y}_{\Psi_\text{d},5}$	$4.207 \cdot 10^{-6}$	$3.036 \cdot 10^{-5}$	$8.840 \cdot 10^{-7}$	$5.780 \cdot 10^{-6}$	$1.748 \cdot 10^{-6}$	$6.750 \cdot 10^{-6}$	231
$\tilde{y}_{\Psi_\text{q},1}$	$1.575 \cdot 10^{-5}$	$8.922 \cdot 10^{-5}$	$4.328 \cdot 10^{-6}$	$2.914 \cdot 10^{-5}$	$8.705 \cdot 10^{-6}$	$3.834 \cdot 10^{-5}$	118
$\tilde{y}_{\Psi_\text{q},2}$	$1.116 \cdot 10^{-5}$	$5.264 \cdot 10^{-5}$	$1.814 \cdot 10^{-6}$	$7.076 \cdot 10^{-6}$	$2.743 \cdot 10^{-6}$	$1.278 \cdot 10^{-5}$	116
$\tilde{y}_{\Psi_\text{q},3}$	$1.005 \cdot 10^{-5}$	$3.781 \cdot 10^{-5}$	$1.941 \cdot 10^{-6}$	$1.200 \cdot 10^{-5}$	$3.716 \cdot 10^{-6}$	$1.391 \cdot 10^{-5}$	61
$\tilde{y}_{t_\text{e},1}$	$8.523 \cdot 10^{-6}$	$5.018 \cdot 10^{-5}$	$3.782 \cdot 10^{-6}$	$1.915 \cdot 10^{-5}$	$6.494 \cdot 10^{-6}$	$2.706 \cdot 10^{-5}$	168
$\tilde{y}_{t_\text{e},2}$	$5.842 \cdot 10^{-6}$	$4.658 \cdot 10^{-5}$	$2.014 \cdot 10^{-6}$	$1.262 \cdot 10^{-5}$	$3.885 \cdot 10^{-6}$	$1.718 \cdot 10^{-5}$	318
$\tilde{y}_{t_\text{e},3}$	$8.531 \cdot 10^{-6}$	$4.671 \cdot 10^{-5}$	$3.855 \cdot 10^{-6}$	$1.934 \cdot 10^{-5}$	$6.587 \cdot 10^{-6}$	$2.087 \cdot 10^{-5}$	64

FEM evaluations), making it impossible on a standard computer and necessitating parallel and high-performance computing.

In Approach 2, the direct optimization was performed by incorporating CE-FEM, RBF interpolation, and halving the FEM model's geometry. The computation time and the number of evaluations were reduced by a factor of 10^4 compared to Approach 1. However, performing one MOO with Approach 2 would still require $t_{\Sigma,\text{FEM}} \approx 29.6$ days.

To overcome this, Approach 3 replaced FEM evaluations with multiple ANN-based meta-models. Table 3 presents the corresponding results for the ANN-based optimization approach, with a breakdown of time spent on data collection, ANN training, and MOO. While the initial data collection, which involved FEM evaluation, was time-consuming, the computational cost of ANN training and MOO was negligible compared the FEM-based approach.

The ANNs used in the proposed approach had only three hidden layers, making them computationally efficient. Once trained, ANN-based optimization was highly efficient. The total computation time was $t_{\Sigma,\text{ANN+data}} \approx 1.57$ days, primarily due to the FEM-based data collection, while the actual optimization process required only $t_{\Sigma,\text{ANN}} \approx 2.25$ h. Comparing Approaches 2 and 3 showed a further reduction in computation time by a factor of approximately 20 in the case of the first optimization attempt.

Furthermore, a key advantage of Approach 3 is that it allows for multiple optimization runs with different objectives and constraints without requiring additional FEM evaluations, if the objective functions involve the modeled variables (i.e., flux linkage and torque maps), making it highly practical for real-world applications. Additionally, this concept is evaluated in Approach 4, where optimization is repeated without the need for additional data collection and training, demonstrating the efficiency and adaptability of ANNs in various optimization scenarios. This enables fine-tuning of MOO objectives and constraints in an iterative process, as discussed in Section 2.3. Using Approach 4 for various MOO scenarios that are based on the discussed nonlinear maps further significantly reduces overall computation time compared to Approaches 1 and 2.

6.1.1. Computational complexity

The computational complexity was assessed for the FEM and ANN-based models, as they are central in the MOO iterative evaluation. The computational complexity of the current-driven magnetostatic FEM model (solving a nonlinear problem using Newton–Raphson) is generally defined by $\mathcal{O}(k N_\text{dof}^2)$. The total number of degrees of freedom N_dof is defined by the number of finite elements multiplied by the degrees of freedom per element, and k represents the number of Newton iterations. The FEM model consisted of more than 5000 elements, each with 6 degrees of freedom, therefore, the polynomial complexity resulted in a very high computational cost.

The computational complexity of the ANN model, with 8 input neurons, three hidden layers (20, 30, and 10 neurons), and one output neuron, is primarily determined by matrix multiplications in the fully connected layers. The complexity is approximately $\mathcal{O}\left(\sum_{i=0}^{N_\text{l}} N_{\text{neu},i} N_{\text{neu},i+1}\right)$, where $N_\text{l} = 3$ is the number of layers, and $N_{\text{neu},i}$ represents the number of neurons in layer i. Layer 0 corresponds to the input layer, and layer 4 corresponds to the output layer. Since the most computationally expensive layer dominates in a fully connected network, the complexity can be approximated by $\mathcal{O}(N_\text{l} N_{\text{neu,max}}^2)$, where $N_{\text{neu,max}}$ is the maximum number of neurons in any layer.

Although both models exhibit polynomial complexity, the ANN model is far more efficient in practice, as the total number of neurons is significantly smaller than the total number of degrees of freedom in the FEM model. This results in orders of magnitude lower computational cost. Specifically, the FEM model corresponds to $\mathcal{O}\left(10^{10}\right)$, whereas the ANN model corresponds to $\mathcal{O}\left(10^3\right)$. Furthermore, a single ANN evaluation effectively replaces five FEM model evaluations, further reducing the overall computational cost of the ANN-based approach.

6.2. Accuracy and generalization of ANNs

Table 4 compares the proposed ANN approach with the State-of-the-Art Kriging method (MathWorks, 2025; Sun et al., 2021), using MSE as a measure of predictive accuracy. For each intermediate data, the MSE is reported separately for training, validation, and test datasets for the ANNs. Additionally, the total MSE for ANN training, which includes both training and validation data, is provided. This enabled comparison with Kriging, where the model formulation is based on both training and validation data. Both models were also evaluated on the test dataset, ensuring a comparison of their performance. For the ANN models, the number of training epochs is also presented, to give more

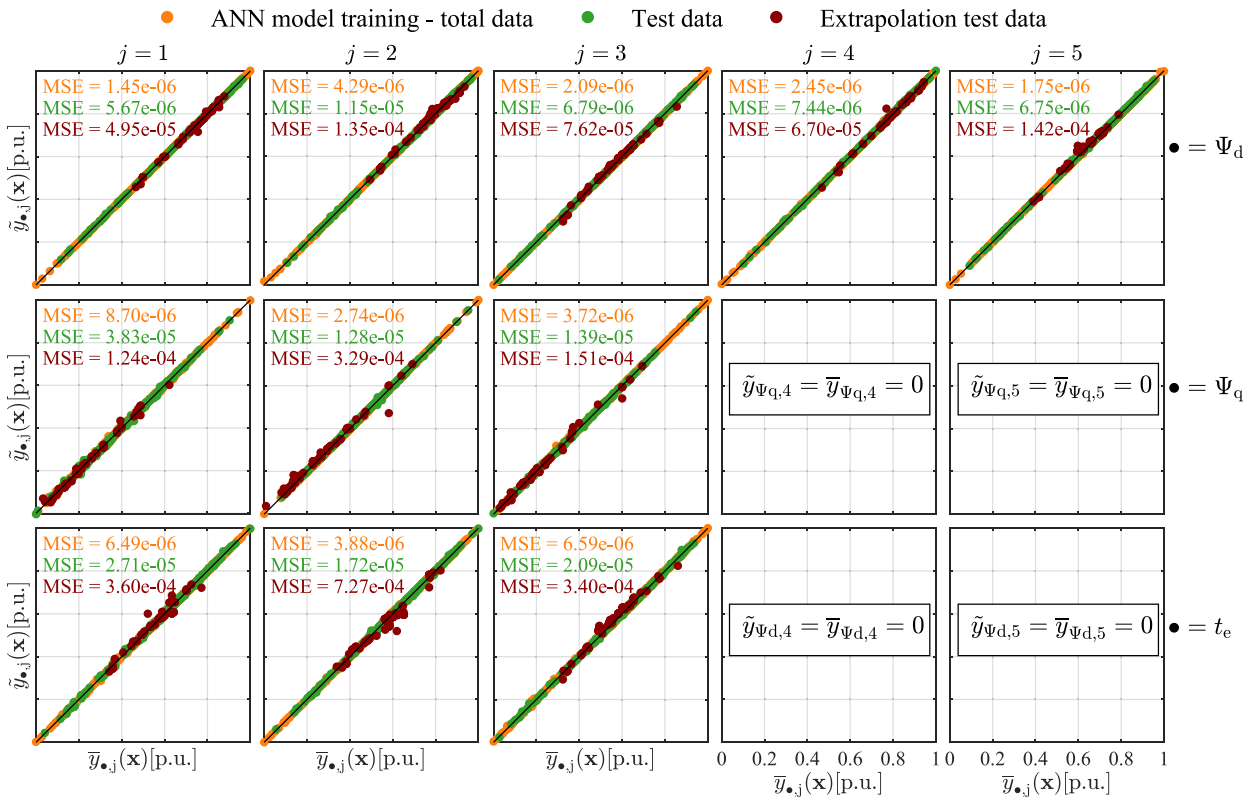

Fig. 6. Regression plots for all ANNs with MSE.

detail on the data-driven model optimization process and the model convergence.

The comparison focused on test data performance (highlighted in gray in Table 4). The ANN-based models consistently outperformed the Kriging model on test data. Furthermore, when comparing the total MSE from ANN model training with the MSE of the data used for Kriging model formulation (i.e., both based on the same dataset), the ANNs demonstrated more accurate performance. The greatest difference in test data performance was observed for the intermediate variable $\tilde{y}_{\Psi_d,1}$, where the ANN model achieved an MSE of $5.674 \cdot 10^{-6}$, significantly lower than the $2.991 \cdot 10^{-5}$ obtained by the Kriging model. The results confirmed that the ANN-based meta-model was more accurate and was a reliable alternative to the State-of-the-Art Kriging model for predicting unseen data.

The performance, accuracy, and generalization ability of the ANNs are presented in Fig. 6 by using normalized regression plots, which present how the ANNs output $\tilde{y}_{\bullet,j}$ correspond to the FEM-based outputs $\overline{y}_{\bullet,j}$. In addition, corresponding MSEs are presented to provide a quantitative evaluation of the performance of the ANNs.

Eleven intermediate data values were modeled using ANNs, while values in 4 OPs were considered zero. Since the flux linkage in the q-axis Ψ_q and the electromagnetic torque t_e at OPs 4 and 5 always resulted in zero, as shown in Fig. 3, there was no need to model these points with ANNs. The fact that $\overline{y}_{\Psi_q,j}$ and $\overline{y}_{t_e,j}$ in OP $j = 4$ and $j = 5$ result in zero is a characteristic inherent to all types of IPMSM. This property was leveraged to minimize the number of ANNs required within the MOO process.

For each ANN, three regression plots are shown. The first, displayed in orange, represents the combined regression of the training and validation datasets (i.e., ANN model training), consisting of 1275 samples (i.e., 85% of the total data sets). The second, displayed in green, represents the regression of the test datasets, consisting of 225 samples (i.e., 15% of the total data sets). All data points in the training, validation, and test datasets fall within the defined upper and lower limits of $\boldsymbol{x}$. The third regression plot, displayed in red, presents the ANN's generalization ability (i.e., their extrapolation ability) to predict intermediate data for cases beyond the upper and lower limits of $\boldsymbol{x}$. 100 samples were generated by varying up to two design variables, setting them 10% above or below their upper and lower limits while keeping the remaining variables at their reference values. If all variables were simultaneously extended beyond the defined limits, the evaluated machines would result in unrealistic designs.

All 11 ANN models exhibited high accuracy during ANN model training (including both training and validation data), as reflected in the MSE values. Notably, all of the ANN models achieved MSE values in the order of 10^{-6}. While the accuracy of the ANNs on the test data was lower compared to the training accuracy, the MSE values remained low, ranging from 10^{-5} to 10^{-6}. Training the ANNs separately for each intermediate dataset resulted in accurate meta-models across all data types, regardless of the selected OP. For unlearned cases outside the limits of $\boldsymbol{x}$, the accuracy of the ANNs decreased compared to predictions within the defined range. Nevertheless, across the given samples, the MSE for all ANNs remained within 10^{-4} to 10^{-5}, demonstrating their ability to provide reasonable predictions beyond the predefined upper and lower limits.

6.3. Pareto front evaluation

To assess the quality of the obtained Pareto front, the normalized HI k_{HI} was employed. The computation of the HI was performed using the implementation presented in Fonseca et al. (2008), which normalizes the Pareto front relative to the reference point.

Since the hypervolume is computed as a fraction of the total reference volume, the indicator is bounded between 0 and 1, where $k_{HI} = 1$ indicates that the solution set fully dominates the reference space, and $k_{HI} = 0$ means no dominance. Fig. 7 presents the change of the HI k_{HI} during the ANN-based MOO process. The initial generations exhibited a rapid increase in the HI. Further, the growth decelerated, eventually

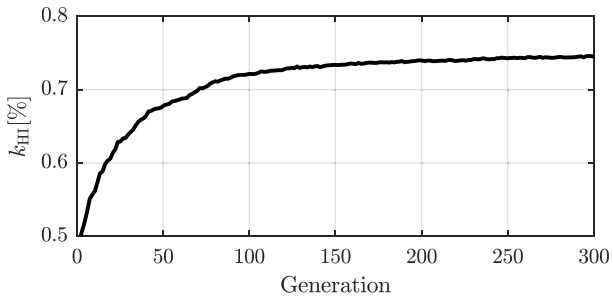

Fig. 7. Evolution of the normalized HI k_{HI} throughout the MOO process.

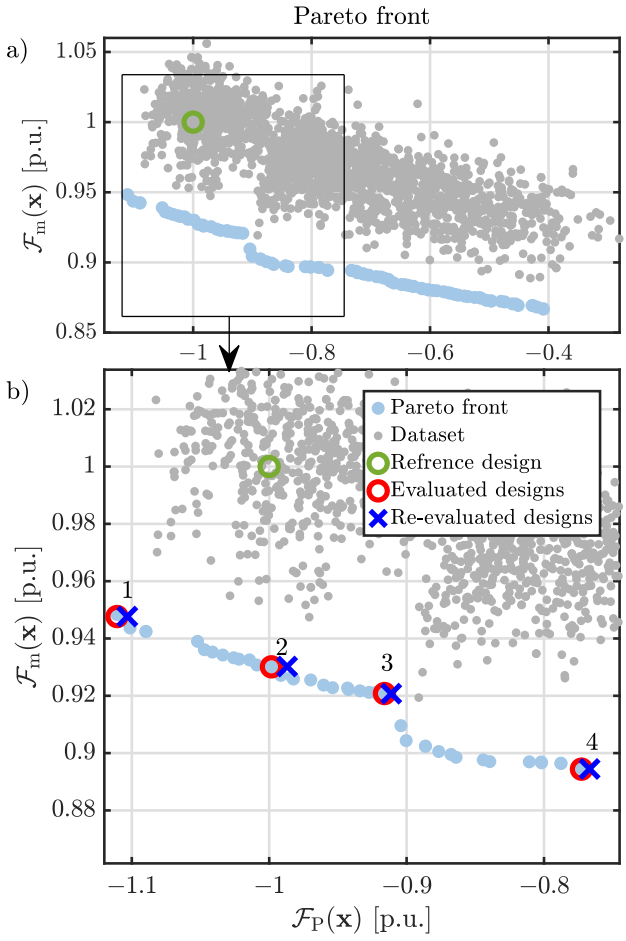

Fig. 8. (a) Full search space with Pareto front and (b) zoomed area of interest: Pareto front with search space and evaluated and FEM-based numerical re-evaluated designs highlighted.

reaching a maximum of 0.7458, indicating convergence towards an optimal Pareto front.

The obtained Pareto front of the ANN-based MOO and the search space corresponding to the design variable matrix $\boldsymbol{X}$ are shown in Fig. 8(a). A zoomed-in view, highlighting the cross-section of interest around the reference design, is provided in Fig. 8(b). To evaluate the accuracy of the Pareto front, selected Pareto solutions were re-evaluated with the FEM-based numerical workflow presented in Fig. 4(a), (c) and (d) and were compared to the Pareto front. The comparison is presented in Fig. 8(b).

The obtained optimized solution set (i.e., the Pareto front) provided different designs, which are all optimal. The objective $\mathcal{F}_P$ offered a range of solutions, increasing power by around 10% and decreasing

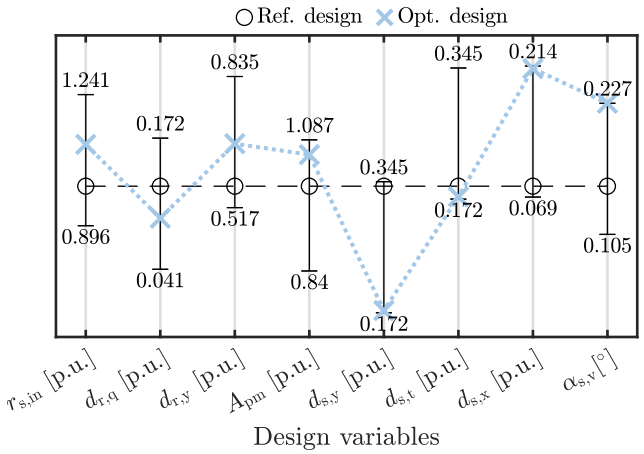

Fig. 9. Geometry parameters of the reference and the selected optimized design (Design 1) relative to the lower and upper limits.

it by over 60% compared to the reference design. The performed MOO reduced mass across all solutions compared to the reference, with reductions ranging from 5% to over 13%. The Pareto front was significantly separated from the main dataset generated for training the ANNs. 4 re-evaluated designs are indicated by numbers in Fig. 8(b) from 1 to 4. When comparing the designs evaluated with ANNs with FEM-based numerically re-evaluated designs, a slight deviation in the objective function $\mathcal{F}_P$ was observed, where $\mathcal{F}_m$ stayed identical, as it was evaluated only analytically. The highest difference of ANN evaluated $\mathcal{F}_P$ compared with the FEM-based numerical evaluated was observed for Design 2, where the difference was 1.1%. While the use of meta-modeling introduced some error in the $\mathcal{F}_P$ evaluation, it did not significantly impact the ANN-based MOO results, allowing advanced MOO to be performed within reasonable timeframes.

Step-like jumps in the Pareto front were observed, linked to the discrete changes in the wire diameter d_w within the performed MOO. An increase in wire diameter d_w permitted a higher maximum current, as defined by (12), which in turn led to an increase in both base torque t_b and power P_b. Consequently also, the slot fill factor was increased, where higher output power correlated with a higher fill factor. Specifically, the slot fill factors were as follows: Design 1 resulted in slot fill factor of 0.73, Design 2 in 0.66, Design 3 in 0.65, and Design 4 in 0.55, respectively. This highlights the correlation between a higher fill factor and increased output power of individual optimized design when applying the presented MOO.

6.4. Evaluation of a selected optimized design

A specific design was selected and evaluated to showcase the improvement achieved with the MOO. Design 1 from the Pareto front (presented in Fig. 8(a)) was selected, as it maximized the base thermal stable base power $\mathcal{F}_P$ and still reduced the mass $\mathcal{F}_m$ compared to the reference design. To evaluate the design changes of the geometry, Fig. 9 and Table 5 present all 8 design variables $\boldsymbol{x}$, where Fig. 9 presents additionally their upper $\boldsymbol{x}_U$ and lower $\boldsymbol{x}_L$ limits. The reference and optimized design variables are presented in comparison with the prescribed limits.

The selected design had an increased rotor $r_{s,in}$ compared to the reference, the magnet cross-section A_{pm} was pushed closer to the upper limit, the tooth $d_{s,t}$ and yoke width $d_{s,y}$ were pushed to the lowest value and the pole shoe tip width $d_{s,x}$ and slot opening angle $\alpha_{s,v}$ were pushed to the upper limits. The rotor parameters $d_{r,q}$ and $d_{r,y}$ settled in the middle of the range. A major improvement was observed in the higher thermal stable base power P_b, which increased by 10.3% compared with the reference value. The total mass m decreased by 5.3%.

Table 5
Geometry parameters of the reference and the selected optimized design (Design 1).

	$r_{s,in}$ [p.u.]	$d_{r,q}$ [p.u.]	$d_{r,y}$ [p.u.]	A_{pm} [p.u.]	$d_{s,y}$ [p.u.]	$d_{s,t}$ [p.u.]	$d_{s,x}$ [p.u.]	$\alpha_{s,v}$ [rad]
Ref.	1	0.124	0.569	1	0.339	0.189	0.081	0.150
Opt.	1.11	0.091	0.672	1.0597	0.175	0.175	0.211	0.227

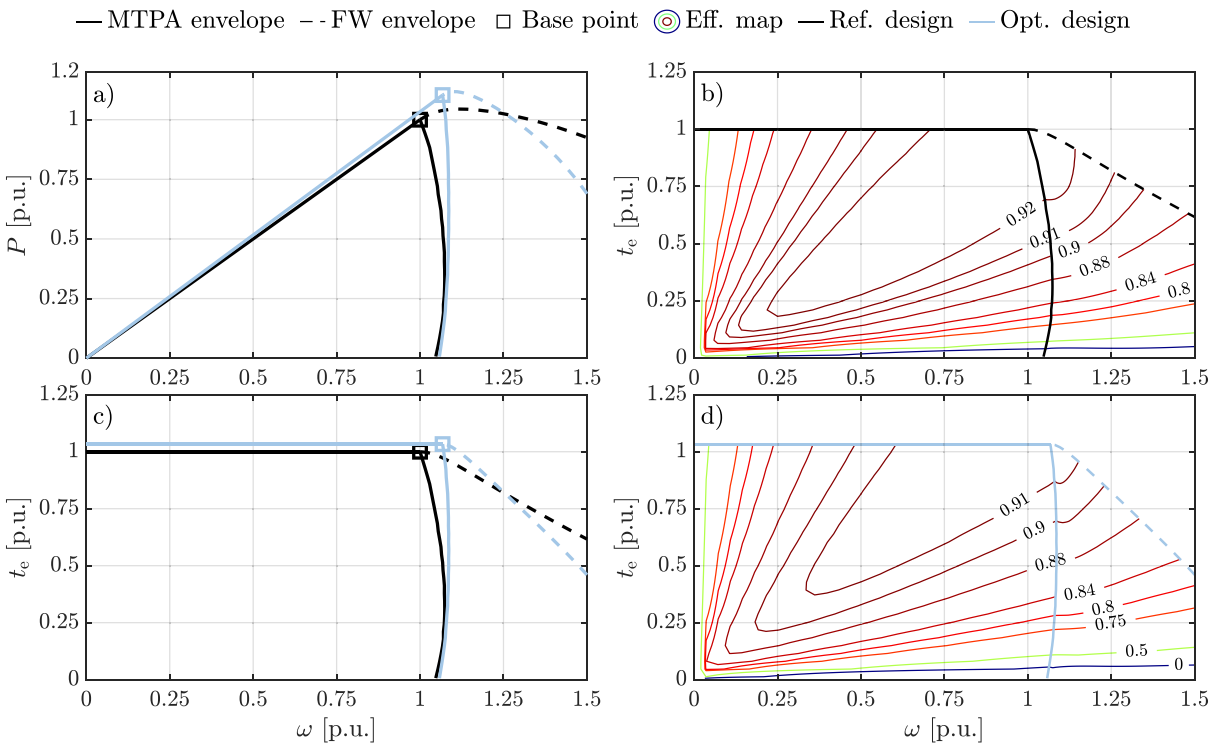

Fig. 10. Operation envelopes and efficiency maps for the reference and the selected optimized design (Design 1): (a) power-speed envelopes, (b) efficiency map of the reference design, (c) torque-speed envelopes, and (d) efficiency map of the optimized design.

This increase of P_b was connected to the bigger magnets and the overall IPMSM layout, which favors high power and allows for the biggest wire diameter d_w. The cooling cross-section was also slightly increased but was below the set limit. The power-to-mass ratio r_P increased for 16.5% compared to the reference, indicating a significant increase in power density achieved through MOO. In the optimized design, the power P_b was increased, due to a combined increase of the maximal torque t_b and base speed ω_b, presented in Fig. 10(a) and (c).

Further, the operating range in terms of speed and torque was expanded in the MTPA region for the optimized design, as shown in Fig. 10(c), which compares the operating envelopes of both designs. The optimized design, on the other hand, showed a decreased FW capability, as the operation limit in the FW region crossed the operation limit of the reference design at $\omega \approx 1.25$ p.u. The optimized design increased the maximal torque limit t_b, which reduced the maximal achievable speed in the FW region (Bianchi et al., 2022). Fig. 10(b) and (d) present the efficiency maps of the reference and optimized designs, respectively. The efficiency of the optimized design decreased compared to the reference design across the entire operating region. The maximum efficiency of the optimized design was reduced to 91%, whereas the reference design achieved a maximum efficiency of 92%. This decrease in efficiency was a drawback of the applied optimization objective, which prioritized increasing power density.

The optimized design was further evaluated thermally using a multi-physics model to verify whether a thermally stable design was achieved with the limitation of the cooling cross-section. The temperature rise of the optimized design at the evaluated $I_{s,max}$ was adequate and resulted in a slightly lower end-winding temperature (127 °C) compared to the reference design. This validated effectiveness of the applied constraint function G_A within the performed MOO.

7. Conclusion

The effective implementation of ANN-based meta-models in the MOO process of IPMSMs was demonstrated through the calculation of a Pareto front, which focused on thermal stable base power increase and mass reduction, including a thermal constraint. The ANNs effectively replaced the FEM-based numerical evaluations required to assess the thermal stable base power of the IPMSM. Instead of directly modeling the objective function with the FEM model, MISO ANNs were used for each intermediate dataset to capture the relationship between the design variables and the average intermediate data generated by the FEM simulations. This approach produced highly accurate meta-models (i.e., ANNs) using a relatively small dataset of 1500 samples, compared to other approaches that require much larger datasets to evaluate intermediate data or KPIs directly (Parekh et al., 2023a,b). To validate the proposed ANN-based MOO framework, a comparison with a State-of-the-Art Kriging-based meta-model was performed, where the proposed ANN-based approach resulted in higher accuracy.

Overall, a significant improvement in computational time and optimization efficiency was achieved. By integrating time-saving strategies, performing the presented MOO was feasible on a standard desktop computer. The use of ANN-based meta-models reduced the total optimization time by a factor of approximately 20 compared to a direct optimization approach in the initial attempt. Another key advantage of the proposed ANN-based approach is the reusability of the trained ANN-based meta-models, allowing multiple optimization scenarios to be conducted without the need for additional time-consuming FEM-based numerical evaluations and iterative fine-tuning of the MOO objective functions and constraints.

The trained ANNs are applicable to the analyzed IPMSM and the defined design variables within the specified limits. While they can be used to some extent beyond these limits, caution is required as accuracy decreases. Nevertheless, the presented approach for modeling the selected machine KPIs (i.e., power and cost) and integrating them into MOO is applicable to other IPMSM designs due to the fully parametrized workflow. Additionally, dedicated ANNs can be trained and evaluated for other permanent magnet or reluctance synchronous machines, further enhancing the method's adaptability and efficiency. Finally, with adequate modifications, the presented approach can also compute additional KPIs, such as efficiency, mass, and etc.

The Pareto front provided a range of optimal solutions for the defined optimization problem. A design was selected based on the performance of the reference machine, achieving improvements in both objectives. For this optimized design, the power-to-mass ratio increased by 16.5% compared to the reference, with a 5.3% reduction in mass m and a 10.3% increase in thermal stable base power P_b. To validate the obtained Pareto front, several selected designs were re-evaluated using the direct FEM-based numerical evaluation. The results showed strong agreement between the FEM-based numerical evaluated and the ANN evaluated designs, with the maximum deviation in thermal stable output power P_b being just 1.1% for Design 2. Further, the quality of the obtained Pareto front was validated by evaluating the hypervolume indicator. The performed comparisons with State-of-the-Art methods for design and optimization of IPMSMs, such as Kriging and direct FEM-based approaches, highlighted the accuracy, flexibility, and computational advantages of the proposed approach.

In future work, we aim to extend the methodology presented by using ANNs to model speed-dependent variables, such as iron losses, further enhancing the optimization process by evaluating efficiency. Additionally, experimental validation will be conducted through the construction of an adequate prototype. In the presented MOO implementation, factors that impact manufacturing feasibility, including minimum bridge thickness in the iron core, discrete changes in commercially available wire sizes, and other practical constraints, were considered. Implementing the optimized design in a physical prototype, however, introduces challenges such as manufacturing tolerances, material property variations, thermal effects, and measurement accuracy, which extend beyond the scope of this research. These factors can impact the demonstrator's performance and the realized benefits of MOO.

CRediT authorship contribution statement

Mitja Garmut: Writing – original draft, Validation, Methodology, Data curation, Writing – review & editing, Visualization, Software, Formal analysis, Conceptualization. **Simon Steentjes:** Validation, Conceptualization, Writing – review & editing, Resources. **Martin Petrun:** Supervision, Project administration, Conceptualization, Writing – review & editing, Resources, Investigation.

Funding

This work was supported by the Slovenian Research and Innovation Agency (ARIS) under Project P2-0115 and Project J7-3152.

Declaration of competing interest

The authors declare the following financial interests/personal relationships which may be considered as potential competing interests: Mitja Garmut reports financial support was provided by Hilti Entwicklungsgesellschaft mbH. Simon Steentjes reports a relationship with Hilti Entwicklungsgesellschaft mbH. that includes: employment. If there are other authors, they declare that they have no known competing financial interests or personal relationships that could have appeared to influence the work reported in this paper.

Data availability

3rd Party Data: Restrictions apply to the availability of these data. Data were obtained from Hilti Entwicklungsgesellschaft mbH, and are available with the permission of Hilti Entwicklungsgesellschaft mbH.

References

Al-Majidi, S.D., Abbod, M.F., Al-Raweshidy, H.S., 2020. A particle swarm optimisation-trained feedforward neural network for predicting the maximum power point of a photovoltaic array. Eng. Appl. Artif. Intell. 92, 103688. http://dx.doi.org/10.1016/j.engappai.2020.103688, URL https://www.sciencedirect.com/science/article/pii/S0952197620301238.

Beume, N., Fonseca, C.M., Lopez-Ibanez, M., Paquete, L., Vahrenhold, J., 2009. On the complexity of computing the hypervolume indicator. IEEE Trans. Evol. Comput. 13 (5), 1075–1082. http://dx.doi.org/10.1109/TEVC.2009.2015575.

Bianchi, N., Carlet, P.G., Cinti, L., Ortombina, L., 2022. A review about flux-weakening operating limits and control techniques for synchronous motor drives. Energies 15 (5), http://dx.doi.org/10.3390/en15051930, URL https://www.mdpi.com/1996-1073/15/5/1930.

Bilgin, B., Liang, J., Terzic, M.V., Dong, J., Rodriguez, R., Trickett, E., Emadi, A., 2019. Modeling and analysis of electric motors: State-of-the-art review. IEEE Trans. Transp. Electrification 5 (3), 602–617. http://dx.doi.org/10.1109/TTE.2019.2931123.

Bramerdorfer, G., Tapia, J.A., Pyrhönen, J.J., Cavagnino, A., 2018. Modern electrical machine design optimization: Techniques, trends, and best practices. IEEE Trans. Ind. Electron. 65 (10), 7672–7684. http://dx.doi.org/10.1109/TIE.2018.2801805.

Brescia, E., Costantino, D., Massenio, P.R., Monopoli, V.G., Cupertino, F., Cascella, G.L., 2021. A design method for the cogging torque minimization of permanent magnet machines with a segmented stator core based on ANN surrogate models. Energies 14 (7), http://dx.doi.org/10.3390/en14071880.

Brown, I.P., Lorenz, R.D., 2007. Response surface methodologies for the design of induction machine self-sensing rotor position saliencies. In: 2007 International Conference on Electrical Machines and Systems. ICEMS, pp. 1354–1359. http://dx.doi.org/10.1109/ICEMS12746.2007.4412061.

Buhmann, M.D., 2003. Radial Basis Functions: Theory and Implementations. Cambridge University Press, Cambridge.

Dianov, A., Tinazzi, F., Calligaro, S., Bolognani, S., 2022. Review and classification of MTPA control algorithms for synchronous motors. IEEE Trans. Power Electron. 37 (4), 3990–4007. http://dx.doi.org/10.1109/TPEL.2021.3123062.

Fonseca, C.M., Paquete, L., López-Ibáñez, M., 2008. Hypervolume indicator. URL https://www.mathworks.com/matlabcentral/fileexchange/19651-hypervolume-indicator, MATLAB Central File Exchange.

Garmut, M., Steentjes, S., Petrun, M., 2022. Parameter identification for MTPA control based on a nonlinear d-q dynamic IPMSM model. COMPEL - Int. J. Comput. Math. Electr. Electron. Eng. 42 (4), 846–860. http://dx.doi.org/10.1108/COMPEL-09-2022-0331.

Garmut, M., Steentjes, S., Petrun, M., 2024a. Evaluating the thermal stability of an interior permanent magnet synchronous machine through iterative multi2010physics simulation. Int. J. Numer. Modelling, Electron. Netw. Devices Fields 37 (5), http://dx.doi.org/10.1002/jnm.3294.

Garmut, M., Steentjes, S., Petrun, M., 2024b. Optimization of an IPMSM for constant-angle square-wave control of a BLDC drive. Mathematics 12 (10), http://dx.doi.org/10.3390/math12101418, URL https://www.mdpi.com/2227-7390/12/10/1418.

Husain, I., Ozpineci, B., Islam, M.S., Gurpinar, E., Su, G.-J., Yu, W., Chowdhury, S., Xue, L., Rahman, D., Sahu, R., 2021. Electric drive technology trends, challenges, and opportunities for future electric vehicles. Proc. IEEE 109 (6), 1039–1059. http://dx.doi.org/10.1109/JPROC.2020.3046112.

Khan, A., Mohammadi, M.H., Ghorbanian, V., Lowther, D., 2020a. Efficiency map prediction of motor drives using deep learning. IEEE Trans. Magn. 56 (3), 1–4. http://dx.doi.org/10.1109/TMAG.2019.2957162.

Khan, A., Mohammadi, M.H., Ghorbanian, V., Lowther, D., 2020b. Efficiencyy map prediction of motor drives using deep learning. IEEE Trans. Magn. 56 (3), 1–4. http://dx.doi.org/10.1109/TMAG.2019.2957162.

Lei, G., Zhu, J., Guo, Y., Liu, C., Ma, B., 2017. A review of design optimization methods for electrical machines. Energies 10 (12), http://dx.doi.org/10.3390/en10121962.

Li, Y., Lei, G., Bramerdorfer, G., Peng, S., Sun, X., Zhu, J., 2021. Machine learning for design optimization of electromagnetic devices: Recent developments and future directions. Appl. Sci. 11 (4), http://dx.doi.org/10.3390/app11041627.

Li, W., Zhang, T., Wang, R., Huang, S., Liang, J., 2023. Multimodal multi-objective optimization: Comparative study of the state-of-the-art. Swarm Evol. Comput. 77, 101253. http://dx.doi.org/10.1016/j.swevo.2023.101253, URL https://www.sciencedirect.com/science/article/pii/S2210650223000275.

Lucchini, F., Torchio, R., Cirimele, V., Alotto, P., Bettini, P., 2022. Topology optimization for electromagnetics: A survey. IEEE Access 10, 98593–98611. http://dx.doi.org/10.1109/ACCESS.2022.3206368.

MathWorks, 2024a. Deep learning toolbox: feedforwardnet. URL https://www.mathworks.com/help/deeplearning/ref/feedforwardnet.html. (Accessed 06 August 2024).

MathWorks, 2024b. Global optimization toolbox: Genetic algorithm and direct search toolbox - gamultiobj. URL https://www.mathworks.com/help/gads/gamultiobj.html. (Accessed 06 August 2024).

MathWorks, 2025. Fitrgp: Train a Gaussian process regression (GPR) model. URL https://www.mathworks.com/help/stats/fitrgp.html. (Accessed 10 March 2025).

Mohanraj, D., Aruldavid, R., Verma, R., Sathiyasekar, K., Barnawi, A.B., Chokkalingam, B., Mihet-Popa, L., 2022. A review of BLDC motor: State of art, advanced control techniques, and applications. IEEE Access 10, 54833–54869. http://dx.doi.org/10.1109/ACCESS.2022.3175011.

Morimoto, S., Sanada, M., Takeda, Y., 1994. Wide-speed operation of interior permanent magnet synchronous motors with high-performance current regulator. IEEE Trans. Ind. Appl. 30 (4), 920–926. http://dx.doi.org/10.1109/28.297908.

Parekh, V., Flore, D., Schöps, S., 2021. Deep learning-based prediction of key performance indicators for electrical machines. IEEE Access 9, 21786–21797. http://dx.doi.org/10.1109/ACCESS.2021.3053856.

Parekh, V., Flore, D., Schöps, S., 2022. Variational autoencoder-based metamodeling for multi-objective topology optimization of electrical machines. IEEE Trans. Magn. 58 (9), 1–4. http://dx.doi.org/10.1109/TMAG.2022.3163972.

Parekh, V., Flore, D., Schöps, S., 2023a. Deep learning-based meta-modeling for multi-objective technology optimization of electrical machines. IEEE Access 11, 93420–93430. http://dx.doi.org/10.1109/ACCESS.2023.3307499.

Parekh, V., Flore, D., Schöps, S., 2023b. Performance analysis of electrical machines using a hybrid data- and physics-driven model. IEEE Trans. Energy Convers. 38 (1), 530–539. http://dx.doi.org/10.1109/TEC.2022.3209103.

Pech, S., Kandler, G., Lukacevic, M., Füssl, J., 2019. Metamodel assisted optimization of glued laminated timber beams by using metaheuristic algorithms. Eng. Appl. Artif. Intell. 79, 129–141. http://dx.doi.org/10.1016/j.engappai.2018.12.010.

Pechlivanidou, M.C., Chasiotis, I.D., Karnavas, Y.L., 2019. A comparative study on 2D and 3D magnetic field analysis of permanent magnet synchronous motor using FEM simulations. J. Electromagn. Waves Appl. 33 (17), 2215–2241. http://dx.doi.org/10.1080/09205071.2019.1674190.

Sasaki, H., Hidaka, Y., Igarashi, H., 2022. Prediction of IPM machine torque characteristics using deep learning based on magnetic field distribution. IEEE Access 10, 60814–60822. http://dx.doi.org/10.1109/ACCESS.2022.3179835.

Sasaki, H., Igarashi, H., 2019. Topology optimization accelerated by deep learning. IEEE Trans. Magn. 55 (6), 1–5. http://dx.doi.org/10.1109/TMAG.2019.2901906.

Shang, K., Ishibuchi, H., He, L., Pang, L.M., 2021. A survey on the hypervolume indicator in evolutionary multiobjective optimization. IEEE Trans. Evol. Comput. 25 (1), 1–20. http://dx.doi.org/10.1109/TEVC.2020.3013290.

Shimizu, Y., 2024. Automatic design system with generative adversarial network and vision transformer for efficiency optimization of interior permanent magnet synchronous motor. IEEE Trans. Ind. Electron. 1–10. http://dx.doi.org/10.1109/TIE.2024.3363768.

Sizov, G.Y., Ionel, D.M., Demerdash, N.A.O., 2012. Modeling and parametric design of permanent-magnet AC machines using computationally efficient finite-element analysis. IEEE Trans. Ind. Electron. 59 (6), 2403–2413. http://dx.doi.org/10.1109/TIE.2011.2163912.

Sun, X., Shi, Z., Lei, G., Guo, Y., Zhu, J., 2021. Multi-objective design optimization of an IPMSM based on multilevel strategy. IEEE Trans. Ind. Electron. 68 (1), 139–148. http://dx.doi.org/10.1109/TIE.2020.2965463.

Vuković, M., Koutroulis, G., Mutlu, B., Krahwinkler, P., Thalmann, S., 2024. Local machine learning model-based multi-objective optimization for managing system interdependencies in production: A case study from the ironmaking industry. Eng. Appl. Artif. Intell. 133, 108099. http://dx.doi.org/10.1016/j.engappai.2024.108099.

Wiens, T., 2024. Radial basis function network. URL https://www.mathworks.com/matlabcentral/fileexchange/22173-radial-basis-function-network. (Accessed 06 August 2024).

Zhao, W., Shen, H., Lipo, T.A., Wang, X., 2018. A new hybrid permanent magnet synchronous reluctance machine with axially sandwiched magnets for performance improvement. IEEE Trans. Energy Convers. 33 (4), 2018–2029. http://dx.doi.org/10.1109/TEC.2018.2876938.

Zheng, S., Zhu, X., Xiang, Z., Xu, L., Zhang, L., Lee, C.H., 2022. Technology trends, challenges, and opportunities of reduced-rare-earth PM motor for modern electric vehicles. Green Energy Intell. Transp. 1 (1), 100012. http://dx.doi.org/10.1016/j.geits.2022.100012.